Feedback from retinal ganglion cells to the inner retina

Authors: Anastasiia Vlasiuk[1,2] and Hiroki Asari[1,3]

Affiliations:

1. European Molecular Biology Laboratory (EMBL), Epigenetics and Neurobiology Unit, Rome, Italy
2. Candidate for Joint PhD degree from EMBL and Heidelberg University, Faculty of Biosciences, Heidelberg, Germany
3. Previous affiliations: Department of Molecular and Cellular Biology and Center for Brain Science, Harvard University, Cambridge, Massachusetts, USA;
   Division of Biology and Biological Engineering, California Institute of Technology, Pasadena, California, USA

Corresponding author: Hiroki Asari, E-mail: asari@embl.it

Acknowledgments: We gratefully acknowledge Markus Meister for assistance with experiments. We also thank all the members of the Asari lab at EMBL Rome as well as Cornelius Gross and Santiago Rompani for many useful discussions.

Grants: This work was supported by Gosney Postdoctoral Fellowship from CalTech and grants from EMBL (H.A.).

Author contributions: A.V. and H.A. designed the study, performed the experiments, analyzed the results, and wrote the manuscript.

Competing interests: The authors declare no competing financial interests.

Abstract

Retinal ganglion cells (RGCs) are thought to be strictly postsynaptic within the retina. They carry visual signals from the eye to the brain, but do not make chemical synapses onto other retinal neurons. Nevertheless, they form gap junctions with other RGCs and amacrine cells, providing possibilities for RGC signals to feed back into the inner retina. Here we identified such feedback circuitry in the salamander and mouse retinas. First, using biologically inspired circuit models, we found mutual inhibition among RGCs of the same type. We then experimentally determined that this effect is mediated by gap junctions with amacrine cells. Finally, we found that this negative feedback lowers RGC visual response gain without affecting feature selectivity. The principal neurons of the retina therefore participate in a recurrent circuit much as those in other brain areas, not being a mere collector of retinal signals, but are actively involved in visual computations.

Acronyms

GABA, γ-aminobutyric acid; GCM, ganglion cell module; LNFDSCNF, linear-nonlinear-feedback-delayed-sum-coupling-nonlinear-feedback; MFA, meclofenamic acid; PSTH, peri-stimulus time histogram; PTX, picrotoxin; RGC, retinal ganglion cell; STR, strychnine.

Introduction

Many brain circuits involve recurrent connections between principal neurons (Ito, 2000; Maass and Markram, 2002; Wang, 2008). This allows for feedback control that can shape the dynamics of neuronal activity, and is suggested to play critical roles in both local and global circuit functions, ranging from sensory information processing to decision making (Carandini and Heeger, 2012).

In the retina, the principal neurons—i.e., ganglion cells—are often thought to be strictly output elements (Gollisch and Meister, 2010; Masland, 2012). Previous studies have thus focused on characterizing how ganglion cells integrate signals from inner retinal neurons distributed in space and across different cell-types via chemical synapses (Berry et al., 1999; Wässle, 2004; Werblin, 2011). As a result, two major mechanisms have been found that are important to control ganglion cell activity: feedforward signaling from bipolar cells to ganglion cells via amacrine cells (Chen et al., 2010; Roska et al., 2006, 2000), and feedback signaling between bipolar cells and amacrine cells (Dong and Werblin, 1998; Nirenberg and Meister, 1997; Tachibana and Kaneko, 1988).

Ganglion cells are, however, part of extensive gap junction networks in the retina (Bloomfield and Völgyi, 2009; Cook and Becker, 1995). While retinal neurons are generally coupled among those of the same type, ganglion cells also form electrical synapses with amacrine cells (Völgyi et al., 2009). Therefore, ganglion cells could in principle signal back to the inner retina to modify the synaptic inputs they receive. Importantly, such feedback control of ganglion cell activity can be both excitatory and inhibitory. On the one hand, excitatory effects are expected from couplings through gap junction networks as they allow for electrical and bidirectional interactions among coupled neurons (Bloomfield and Völgyi, 2009). Different architectures of the gap junction networks are indeed responsible for distinct firing patterns among ganglion cells over multiple time-scales. For example, direct couplings between ganglion cells underlie their nearly synchronous activity within a few milliseconds, whereas indirect couplings via amacrine cells are suggested to mediate the broadly correlated activity of ganglion cells over hundreds of milliseconds (Brivanlou et al., 1998; Mastronarde, 1983; Meister et al., 1995; Trong and Rieke, 2008; Völgyi et al., 2013). On the other hand, inhibitory effects will be obtained if

ganglion cells send feedback signals to amacrine cells through electrical synapses, while the amacrine cells in turn inhibit the ganglion cells through chemical synapses (Greschner et al., 2016; Kenyon and Marshak, 1998; Sakai and Naka, 1988, 1990). The computational power of ganglion cells should then be greater than is commonly thought, allowing for more complex and diverse visual processing. It remains unclear, though, if these feedback pathways are truly functional in the retina, and how they contribute to visual information processing in the retina.

Here we characterized such feedback circuitry in the salamander and mouse retina by combining computational and experimental approaches. Using a circuit model with biologically interpretable elements (Real et al., 2017), we first show that ganglion cells exchange signals with other ganglion cells in two distinct ways: faster, enhancing signals from proximal cells and slower, suppressing signals from distal cells. To experimentally test this model prediction, we perturbed the activity of ganglion cells in the dark by electrically stimulating the optic nerve emerging from an isolated retina, while simultaneously monitoring the consequences of the perturbation by multi-electrode array recordings. Consistent with our model's prediction, the optic nerve stimulation produced a short period of enhanced firing (for tens of milliseconds), followed by a suppression of firing on longer time scales (for hundreds of milliseconds). The slower suppression was largely eliminated by pharmacologically blocking electrical or inhibitory synaptic transmission. Because inhibition is mediated by amacrine cells in the inner retina (Masland, 2012), these results support that ganglion cells form negative feedback circuits with amacrine cells via gap junctions (Greschner et al., 2016; Kenyon and Marshak, 1998; Sakai and Naka, 1988, 1990). Finally, by pairing the nerve shock with visual stimulation, we found that the negative feedback modulates the visual response gain but not the stimulus feature selectivity of ganglion cells, whereas the positive feedback can affect both. Therefore, we conclude that ganglion cells can actively control their own spiking activity and that of other ganglion cells via recurrent connections with amacrine cells, providing additional mechanism for adaptive gain control in the retina.

Results

Circuit models with electrical couplings recapitulate retinal ganglion cell visual responses better than non-coupled models

How do ganglion cells interact with each other in the retina? To address this question, we started with a modeling approach that includes subthreshold effects of electrical couplings between retinal ganglion cells (Bloomfield and Völgyi, 2009; Cook and Becker, 1995). Here we followed the cascade model framework and extended the neural circuit models of Real et al. (2017): specifically, the full "linear-nonlinear-feedback-delayed-sum-nonlinear-feedback" (LNFDSNF) model as well as the reduced "linear-nonlinear-sum-nonlinear" (LNSN) model were employed as a baseline non-coupled model. Briefly, the first LNF stages collectively work as spatial subunits that correspond to bipolar cells and their upstream circuitry; the middle D stage is a delay in lateral propagation introduced by amacrine cells; and the last SNF stages represent the spatial summation by a target ganglion cell (see Methods for details).

Our coupled models (LNFDSCNF and LNSCN; see also Supplementary Figure 1A and Figure 1A, respectively) were then built by incorporating the following two parameters into the non-coupled models. The first parameter is the net coupling strength that represents the effect of both direct coupling between ganglion cells and indirect pathways via amacrine cells (Eq.(2) in Methods). A positive value is expected for a directly coupled pair of ganglion cells (Brivanlou et al., 1998), where the coupling strength largely depends on the number of electrical synapses between the cells and their conductance (Bloomfield and Völgyi, 2009). In contrast, a negative value is expected for an indirectly coupled cell pair, where signals from one ganglion cell transmit to an amacrine cell via electrical synapses and the amacrine cell in turn inhibits the other ganglion cell via chemical synapses (Greschner et al., 2016; Kenyon and Marshak, 1998). The second parameter is the net latency for signals to arrive from the neighboring ganglion cell to the modelled cell (Eq.(1) in Methods). A short latency is expected for a directly coupled pair, whereas a long latency is expected for an indirectly coupled pair. Importantly, here we kept the model size minimum to achieve reliable data fitting, with only two extra free parameters for each surrounding ganglion cell to describe the net effect of its action potentials on a target cell.

Nevertheless, our coupled models are flexible enough to account for the overall effect of the interactions between retinal ganglion cells through the entire circuitry of the inner retina.

When fitted, these coupled and non-coupled models were both able to approximate the firing patterns of salamander (Asari and Meister, 2012, 2014; Real et al., 2017) and mouse (Lefebvre et al., 2008) retinal ganglion cells in response to white-noise visual stimuli consisting of randomly flickering bars (e.g., Figure 1B–D; see Methods for details). The non-coupled models, however, occasionally predicted visual responses at times when they should not, while the coupled models often correctly suppressed such false-positive responses by the firing of negatively coupled cells that have the same response polarity as the target cell (Figure 1C,D). This led to a small but statistically significant improvement of the coupled models in recapitulating the ganglion cell visual responses compared to the non-coupled models (Figure 1E,F; R^2=31.4±9.1 versus 29.7±8.7, p<0.001, for salamander cells; R^2=21.5±8.8 versus 20.8±8.7, p<0.001, for mouse cells; mean ± standard deviation of the coefficient of determination (Eq.(3) in Methods) for the reduced models, paired t-test; see also Supplementary Figure 1B,C for the full models). In contrast, surrounding cells of the opposite response polarities contributed much less to the performance of the coupled models (R^2=32.2±9.5 versus 30.9±10.0, p<0.001, for salamander cells; R^2=20.9±9.0 versus 20.8±8.7, p>0.5, for mouse cells). Importantly, to avoid confounding effects of common visual inputs in the coupled model, we considered only those surrounding cells that have low spike correlations—hence virtually no receptive field overlap—with the target cell (Supplementary Figure 3). Therefore, as suggested by previous anatomical studies (Völgyi et al., 2009), our circuit model analysis supports the presence and solid contributions of couplings between retinal ganglion cells, especially those of the same response polarity, to shaping their visual response dynamics.

Circuit model analysis predicts both positive and negative couplings between retinal ganglion cells

We next analyzed the model parameters to gain insights into the retinal circuits underlying ganglion cell couplings and to derive experimentally testable predictions. The data sets from ON

and OFF cells were combined here as they showed the same trend (Figure 2 and Supplementary Figure 2).

First, we found both positive and negative couplings between ganglion cells of the same response polarities (Figure 2A,B and Supplementary Figure 2A,B for salamander retinas; Figure 2E,F and Supplementary Figure 2E,F for mouse retinas). These couplings were frequently reciprocal, either mutually positive or negative between given cell pairs (Figure 2G,I and Supplementary Figure 2G,I). This indicates that a single ganglion cell can be involved in multiple feedback pathways, imposing distinct effects on different surrounding cells. In contrast, positive couplings dominated between the cell pairs with different response polarities (Figure 2C,D,H for salamander cells; mouse data not analyzed because the coupled model performance did not improve significantly; Figure 1F). Consistently, such a cross-talk between the ON and OFF channels via gap junctions has been reported recently (Cooler and Schwartz, 2020). Taken together, the negative couplings are suggested to be formed exclusively between ganglion cells of the same response polarities.

Second, positive couplings were on average found between cell pairs at a shorter distance and had a shorter latency than negative couplings (Figure 2A–F and Supplementary Figure 2A–F). Because the diameter of ganglion cell dendritic fields is around 0.3 mm (Völgyi et al., 2009; Zhang and Wu, 2010), the distance of the shorter positive couplings (0.31 ± 0.14 and 0.33 ± 0.25 mm for salamander and mouse cell pairs, respectively, median $\pm$ interquartile range from the reduced models) is consistent with direct interactions between ganglion cells, but that of the negative couplings (0.40 ± 0.26 and 0.78 ± 0.74 mm, respectively) exceeds what one expects for direct coupling. The circuit model thus predicts faster enhancing effects between proximal ganglion cells via direct coupling and slower suppressing effects between distal cells via indirect coupling. The prediction on the positive couplings is well supported by previous studies (Brivanlou et al., 1998; Cocco et al., 2009; Pillow et al., 2008), but direct experimental evidence is still lacking on the slow negative coupling between ganglion cells over a long distance (but see, Greschner et al., 2016; Sakai and Naka, 1988, 1990).

Third, there was no marked difference in the common parameters between coupled and non-coupled models (Supplementary Figure 4). Consistently, the outputs of these two models

showed nearly identical dynamics (e.g., Figure 1D), suggesting that the ganglion cell couplings have little effect on the cell's stimulus feature selectivity. Importantly, however, non-desired response peaks were present more frequently in the output of the non-coupled models than that of the coupled models (e.g., Figure 1D). This indicates that the ganglion cell couplings have some transient effects on the response gain of a target cell, suppressing such false-positive responses that were present otherwise.

In summary, our circuit model analysis predicts that, besides bidirectional excitation via gap junction networks (Bloomfield and Völgyi, 2009), retinal ganglion cells of the same response polarity can have reciprocal indirect inhibition between each other for a transient gain control from outside their receptive fields.

Optic nerve stimulation imposes diverse effects on ganglion cell activity

To directly test the model prediction of an indirect inhibition between retinal ganglion cells (Figures 1 and 2 and Supplementary Figures 1–4), we next experimentally examined how the firing patterns of ganglion cells are affected by their own action potentials and the action potentials of other ganglion cells. Here we sought to perturb the activity of many ganglion cells simultaneously to strongly drive the recurrent signaling pathways, but in a manner independent of light signaling pathways. We thus electrically stimulated the optic nerve emerging from an isolated retina in the dark and simultaneously recorded the spiking activity of ganglion cells to monitor the outcome of the perturbation (Figure 3A). A decrease of the firing rates should follow the nerve stimulation if ganglion cells are part of the proposed negative feedback circuitry, whereas no significant change should be observed if the stimulated cells are all purely postsynaptic within the retina.

We found that the optic nerve stimulation had pronounced effects on the spontaneous activity of ganglion cells in both salamander and mouse retinas (Figure 3 and Supplementary Figure 5). About a third of the recorded cells showed immediate antidromic spikes after the nerve shock (75 out of 193 salamander cells with spontaneous activity >1 Hz, Figure 3B,C; 41 out of 132 mouse cells, Supplementary Figure 5A,B). In either cells with or without antidromically evoked spikes, we frequently observed a period of enhanced firing over tens

of milliseconds (59 salamander cells, Figure 3D; 20 mouse cells, Supplementary Figure 5B). This fast positive feedback must be mediated by gap junction networks involving both direct and indirect couplings (Bloomfield and Völgyi, 2009; Brivanlou et al., 1998) because ganglion cells do not make chemical synapses within the retina (Masland, 2012). Less frequently, we also observed a suppression of firing on a longer time scale over hundreds of milliseconds (41 salamander cells, Figure 3C,D; 5 mouse cells, Supplementary Figure 5A,B). This slow negative feedback must be mediated by inhibitory amacrine cells in the inner retina because gap junctional networks transmit only sign-conserving signals. The proportion and time course of these indirect enhancing and suppressing effects varied greatly between ganglion cells (Figure 3E and Supplementary Figure 5C). These results support the model prediction that ganglion cells can drive both positive and negative feedback signaling in the inner retina.

Recurrent circuits from retinal ganglion cells involve gap junctions and amacrine cells

What are the retinal circuits underlying such recurrent signaling from ganglion cells? Previous anatomical and computational studies suggest that ganglion cells can form a recurrent circuit with amacrine cells via gap junctions (Bloomfield and Völgyi, 2009; Kenyon and Marshak, 1998; Völgyi et al., 2009). Here we took a pharmacological approach in the salamander retina to test this circuit hypothesis. We first blocked gap junctions by applying 100 μM meclofenamic acid (Zhang and Wu, 2009). This generally led to an elimination of the slow suppressing effects after the nerve shock in the dark (7 out of 8 cells; p=0.036, Fisher's exact test; Figure 4). In contrast, the drug application had little effect on the fast enhancing effects presumably because the drug failed to fully block gap junction networks. Nonetheless, electrical synapses were found indispensable for the negative feedback signaling from ganglion cells. To test the involvement of amacrine cells, we next blocked γ-aminobutyric acid (GABA) and glycine transmission by applying 100 μM picrotoxin and 1.0 μM strychnine. We found that these inhibitory transmission blockers also abolished the suppressing effects after the nerve stimulation in the dark (7 out of 7 cells; p=0.008, Fisher's exact test; Figure 5), while the enhancing effects remained intact. Taken together, these results suggest that the negative

feedback pathway from ganglion cells to amacrine cells via gap junctions is physiologically functional.

Negative feedback signaling modulates gain but not selectivity of ganglion cell visual responses

Thus far we have electrophysiologically examined the negative feedback without presenting visual stimuli. But, how does it affect the visual response properties of retinal ganglion cells? Our model predicts a role in transiently controlling the response gain (Figure 1D). To experimentally test this, we next presented white-noise visual stimuli in combination with the optic nerve stimulation, and exploited the reverse-correlation methods to systematically examine changes in the response gain and feature selectivity of individual cells due to the nerve stimulation (Figure 6A; Chichilnisky, 2001; Wu et al., 2006). Specifically, we fitted a linear-nonlinear (LN) cascade model to the visual responses of each cell at different time points from the nerve shock, and assessed i) the feature selectivity by an ON-OFF index, defined as the difference of the peak and valley values of the linear filter, normalized by the sum of the two (see Eq.(4) in Methods for details); and ii) the response gain by a sigmoid function fitted to the profile of the static nonlinearity from the LN model (Eqs.(5)–(6) in Methods). In the present experiments, due to the presence of the stimulation pipette, we could not avoid a distortion of the visual stimuli projected from above the retina. Our analysis is thus limited to the full-field response properties, but not extended to the spatio-temporal properties.

During a period of suppressed firing after the nerve shock (Figure 6B and Supplementary Figure 6A), the profile of the linear filter largely remained the same (Figure 6C and Supplementary Figure 6B). In contrast, it sometimes showed a marked change during a period of enhanced firing: e.g., from monophasic (having one positive or negative phase) to biphasic (having both positive and negative phases; Supplementary Figure 6A). Consistently, the ON-OFF indices over the population varied significantly more during the period of enhanced firing than during suppressed firing periods (p=0.03, F-test; Figure 6E and Supplementary Figure 6D). This suggests that the feature selectivity of ganglion cells is affected more strongly by the positive feedback than by the negative feedback.

The response gain, in contrast, was affected during both periods of enhancement and suppression after the nerve stimulation (Figure 6D,F,G and Supplementary Figure 6C,E,F). On the one hand, the static nonlinear gain function was generally up-regulated during a period of enhancement (Figure 6F,G and Supplementary Figure 6C,E,F). In particular, the lower bound spike probability showed a significant increase over the population (p<0.001, sign-test, from the salamander data, Figure 6G; see also Supplementary Figure 6C,F). On the other hand, the gain was typically down-regulated during a period of suppression (Figure 6D,F,G and Supplementary Figure 6C,E,F), with a significant decrease of the upper bound spike probability over the population (p<0.001 from the salamander data, Figure 6D,F; see also Supplementary Figure 6C,E). Taken together, these results indicate that the negative feedback signals primarily contribute to modulating the response gain, while ganglion cells may adaptively change their visual response properties by exploiting the whole recurrent circuitry.

Discussion

Circuit modeling is a powerful approach to integrate brain anatomy and physiology for better understanding the overall function of the system (Herz et al., 2006). By explicitly representing individual neurons and their connections with the model parameters, circuit models can provide predictions on the structure and function of the target neuronal circuitry, and subsequently these predictions can be tested by experiments (Real et al., 2017). Here we took this theory-driven approach to functionally characterize the ganglion cell feedback circuits in the inner retina. We first extended a retinal cascade model (Real et al., 2017) to incorporate interactions between ganglion cells as suggested by anatomical studies (Völgyi et al., 2009), and derived a prediction that retinal ganglion cells of the same response polarity form reciprocal inhibition over a long distance for a transient gain modulation (Figures 1–2 and Supplementary Figures 1 and 3). We then experimentally validated that ganglion cells can indeed suppress the firing among themselves by propagating signals to amacrine cells via gap junctions (Figures 3–5 and Supplementary Figure 5). Furthermore, as predicted by our circuit model, we showed that this negative feedback lowers the visual response gain without much affecting the stimulus feature

selectivity of the cells (Figure 6 and Supplementary Figure 6). The discovery of this new gain control mechanism in the retina not only highlights the importance of gap junctions in visual processing, but also promises that theory-driven approaches will further reveal neural circuit functions in future studies.

Retinal gap junction networks have been well conserved across species over evolution (Völgyi et al., 2013). In both salamander and mouse retinas, our circuit model analysis indeed showed the presence of negative couplings among some distal ganglion cells, whereas positive couplings were found more frequently among proximal cells (Figure 2 and Supplementary Figure 2). This spatial organization is consistent with previous studies in both salamander (Cocco et al., 2009) and primate retinas (Greschner et al., 2016; Pillow et al., 2008). Moreover, ganglion cells in both salamander and mouse retinas showed a period of suppression following the optic nerve stimulation under the *ex vivo* condition (Figure 3 and Supplementary Figure 5). Such suppression was also reported in the catfish retina (Sakai and Naka, 1988, 1990) as well as in the primate retina (Gouras, 1969), although the time scale in these previous reports was shorter than that in this study. Nevertheless, later modelling (Kenyon and Marshak, 1998) and correlation-based experimental studies (Greschner et al., 2016) support that such suppression arises from the recurrent circuitry involving amacrine cells via gap junctions, rather than a transient after-hyperpolarization due to the antidromic spikes evoked by the optic nerve stimulation. Taken together, recurrent circuits from retinal ganglion cells are likely present widely across species.

In this study, we employed an optic nerve stimulation to perturb ganglion cell activity independently of the light signaling pathway (Figure 3A). This successfully drove antidromic spikes in many ganglion cells in a time-locked manner (e.g., Figure 3B) and the obtained results largely supported our model predictions on ganglion cell coupling properties. There are, however, some caveats, such as a potential activation of efferent axons from the brain to the retina (Koves et al., 2016; Repérant et al., 2006). Previous studies suggest that dopaminergic amacrine cells receive such centrifugal inputs under the control of circadian rhythms (Gastinger et al., 2006). Although dopamine can affect gap junction networks at nearly every stage of retinal processing, the kinetics are much slower than the time scales considered in this study

(∼100 ms) (Pereda et al., 2013; Roy and Field, 2019; Witkovsky and Dearry, 1991). The effects of the efferent signaling, if any, should thus be negligible on the outcome of the nerve stimulation we observed. These dopaminergic amacrine cells are also suggested to receive direct inputs from intrinsically-photosensitive retinal ganglion cells via axon collaterals (Zhang et al., 2012, 2008). For the same reason, however, the contribution of this dopaminergic pathway should also be minimal in this study.

Another caveat is that the optic nerve stimulation led to an extensive perturbation of the coupling pathways due to a strong synchronous activation of ganglion cell populations (Figure 3 and Supplementary Figure 5). This may explain why the measured effect of the negative feedback lasted long, over hundreds of milliseconds (Figure 3 and Supplementary Figure 5) as opposed to tens of milliseconds in the model predictions (Figure 2 and Supplementary Figure 2). Single-cell stimulation, however, can be too weak to reveal any indirect negative interaction among ganglion cells (Mastronarde, 1983; Trong and Rieke, 2008; but see Sakai and Naka, 1988, 1990). It is a future challenge to further investigate the circuit mechanisms under more physiological conditions and test remaining model predictions, such as reciprocal negative couplings between retinal ganglion cells of the same response polarity (Figure 2G–I and Supplementary Figure 2G–I).

Recurrent normalization plays important roles in many brain functions (Carandini and Heeger, 2012). Consistent with the previous study in the primate retina (Greschner et al., 2016), both our computational model and experimental data show that the ganglion cell recurrent network plays a role in controlling the visual response gain in both salamander and mouse retinas (Figure 6 and Supplementary Figure 6). Interestingly, the interactions between ganglion cells extend over a wide spatial range (up to ∼1 mm; Figure 2 and Supplementary Figure 2) well beyond the extent of their dendritic fields (Völgyi et al., 2009; Zhang and Wu, 2010). Moreover, this gain control mechanism works on a slower time scale (∼100 ms), if not the slowest (Wark et al., 2009), than many other local gain control mechanisms in the retina, such as the synaptic adaptation achieved at bipolar cell terminals at the cellular level (Euler et al., 2014; Matthews, 1999), or negative feedback loop among bipolar cells and amacrine cells at the circuit level (Dong and Werblin, 1998; Nirenberg and Meister, 1997; Tachibana and Kaneko,

1988). Therefore, the ganglion cell feedback circuit likely contribute to slowly equalizing the response gain across populations, but not mediating visual functions that need precise spike timing of individual cells (Geffen et al., 2007; Gollisch and Meister, 2008; Van Rullen and Thorpe, 2001; Victor, 1999). To investigate the structure and function of the feedback circuits for each ganglion cell type, future studies will benefit from further elaborations on the circuit models combined with calcium or voltage imaging techniques to monitor the subcellular activity of individual neurons and trace signal flow within the retina (Baden et al., 2016; Franke et al., 2017).

Methods

No statistical method was used to predetermine the sample size. The significance level is 0.05 (with Bonferroni correction where appropriate) in all analyses unless noted otherwise. All experiments were performed in strict accordance with the protocols approved by the Institutional Animal Care and Use Committee at Harvard University or California Institute of Technology, or under the license 233/2017-PR from Italian Ministry of Health. The data analysis and circuit modeling were done in Matlab (Mathworks) and Python. All data and codes are available upon request.

Modeling

We first reanalyzed the data sets in Asari and Meister (2012, 2014) and Real et al. (2017) for the salamander retinal ganglion cells and those in Lefebvre et al. (2008) for the mouse ganglion cells. Specifically, we focused on the responses to the random noise stimulus consisting of a 1-dimensional array of adjacent bars 8.3–80 μm in width. The light intensities of these bars were drawn from a binary black-or-white distribution (luminance range 0.5–36 mW/m^2), and changed simultaneously, independently, and randomly with a refresh rate of 60–100 Hz.

The distance between the cells (Figure 2 and Supplementary Figure 2) was calculated from the receptive field centers. The spatiotemporal receptive fields of the cells (10–17 ms bin size; 0.4 s window) were estimated by reverse-correlation methods using randomly flickering

checkerboard stimuli (30–83 μm square fields; 60–100 frames/s), and their center location was estimated by the 3-dimensional Gaussian curve fit. Cells with positive receptive field center values were classified as ON cells, whereas those with negative values as OFF cells.

Data selection

The raw data sets contained 479 ganglion cells from 10 isolated salamander retinas, and 35 ganglion cells from a mouse retina. Of those, 185 OFF and 4 ON salamander cells and 10 ON and 12 OFF mouse cells were selected for the subsequent modeling analyses according to the following criteria.

1. Cells should have a high spike sorting quality. To ensure low false positives, cells with $>15\%$ of spikes with <1.7 ms inter-spike intervals were discarded. To ensure low false negatives, cells with nearly identical spatiotemporal receptive field profiles were eliminated except for the one with the highest spike counts.

2. Cells should respond well to the visual stimulus for robust model fitting, assessed by the spike counts during the stimulus presentation period and the performance of a linear-nonlinear (LN) cascade model (Chichilnisky, 2001; Wu et al., 2006). The LN model was fitted by reverse-correlation methods, and cells with $<3{,}000$ spikes and $<10\%$ LN model prediction (coefficient of determination; see below Eq.(3)) were discarded.

3. Cells should have little response correlation due to common visual inputs for modeling interactions between cells. Neighboring cells were included in the coupling models (see below Model formalism) only if Pearson correlation between their spike trains and those of the target cell was low (between -0.1 and 0.1; Supplementary Figure 3). This generally resulted in no overlap of the receptive field centers (e.g., Figure 1B).

Model formalism

We employed the cascade model framework as described in Real et al. (2017). As a non-coupled model (Figure 1 and Supplementary Figures 1 and 4), we thus used the so-called "linear-nonlinear-feedback-delayed-sum-nonlinear-feedback" (LNFDSNF) or full model, and

the "linear-nonlinear-sum-nonlinear" (LNSN) or reduced model. In short, the first LNF stages collectively work as spatial subunits of upstream bipolar cells (Bipolar Cell Modules; Eq.(S3)–(S7) in Real et al., 2017); the middle D is a delay due to lateral signal propagation via amacrine cells (Amacrine Cell Modules; Eq.(S8) in Real et al., 2017); and the last SNF stages represent the spatial summation by a target ganglion cell (Ganglion Cell Modules; GCM; Eq.(S9) in Real et al., 2017), followed by the cell's output nonlinearity (Eq.(S6') below) and the feedback (Eq.(S7) in Real et al., 2017). Here we replaced the Eq.(S6) in Real et al. (2017) with the following formula:

$$y(t) = \begin{cases} 0, & \text{if } z(t) \leq \theta \\ \alpha(z(t) - \theta), & \text{otherwise,} \end{cases} \tag{S6'}$$

where α and θ are the slope and threshold of a half-wave rectification function, respectively. The GCM nonlinearity was thus equipped with two free parameters in this study (Supplementary Figure 4), while it was fixed in Real et al. (2017), equivalent to $\alpha = 1$ and $\theta = 0$ in Eq.(S6').

A full coupling model (LNFDSCNF; Supplementary Figure 1A) and a reduced one (LNSCN; Figure 1A) were then built by introducing the coupling step (C) before the GCM nonlinearity (N) and feedback (F). Specifically, the coupling effects on a target ganglion cell were modelled as a delayed weighted sum of the neighboring ganglion cell activities. For each k-th neighboring cell, two free parameters were hence assigned: l_k for the latency of the signal transmission and a_k for the coupling strength. The latency parameter l_k is non-negative and treated as a delay function that requires interpolation of the measured firing rate $r_k(t)$ of the k-th neighboring cell. The delayed activity $r_k^*(t)$ is thus given as:

$$r_k^*(t) = (1 - \{l_k\})\, r_k(t - \lfloor l_k \rfloor) + \{l_k\}\, r_k(t - \lfloor l_k \rfloor - 1), \tag{1}$$

where $\lfloor l_k \rfloor$ is the largest integer not greater than l_k, and the fractional part $\{l_k\} = l_k - \lfloor l_k \rfloor$. The delayed activity $r_k^*(t)$ is then weighted by a coupling strength a_k and added to the signal $x(t)$ coming from the previous summation (S) step (Eq.(S9) in Real et al., 2017):

$$y(t) = x(t) + \sum_k a_k r_k^*(t). \tag{2}$$

The resulting signal $y(t)$ is in turn used as an input to the following GCM nonlinearity (Eq.(S6')) and feedback steps (Eq.(S7) in Real et al., 2017) to obtain an estimated firing rate of the target cell (e.g., Figure 1).

Model fitting and assessment

We wrote custom codes in Python to fit the models to the ganglion cell firing rates (bin size, 1/100–1/60 s) in response to the randomly flickering bar stimuli. For each cell, we fitted the coupled models in two configurations (Figures 1 and 2 and Supplementary Figures 1–4): the one including only those surrounding cells of the same response polarity as the target cell (e.g., OFF target cell with OFF surrounding cells), and the other with those of different response polarities alone (e.g., OFF target cell with ON surrounding cells).

Model performance was assessed by the coefficient of determination between the measured ganglion cell firing rate $r(t)$ and the model prediction $\hat{r}(t)$:

$$R^2 = 1 - \frac{\sum_t (r(t) - \hat{r}(t))^2}{\sum_t (r(t) - \langle r(t) \rangle)^2}. \tag{3}$$

where $\langle \cdot \rangle$ denotes the mean. It reaches its maximum of 1 in the case of an exact agreement between the two binned sequences, and is around 0 or less in the case of unrelated sequences. Paired t-test was used to compare the model performance with and without couplings (Figure 1E,F and Supplementary Figure 1B,C). Because the coupled model did not improve its performance for mouse cells with surrounding cells of different response polarities, this data set was excluded from the subsequent model parameter analyses (Figure 2 and Supplementary Figures 2–4).

To avoid over-fitting, the model parameters were optimized using a training data set ($\sim$80% of the data) and the model performance was evaluated on a separate testing data set. The testing data set for the salamander data included 8–12 repeats of the identical flicker sequence, and hence the model's output was compared to the average firing rate over all these trials.

Model analysis

We ran a shuffling analysis to evaluate the noise level of the coupling parameters in the LNSCN and LNFDSCNF models (lower and upper thresholds at 0.5 and 99.5 percentiles, respectively; Figure 2 and Supplementary Figure 2). Specifically, for each modelled cell, we fitted the model parameters to its true spike trains together with randomly jittered spikes trains from all coupled neighboring cells. This keeps intact the stimulus-dependence of the modelled cell's response, but breaks the correlation to the responses of the other cells. Thus the obtained coupling parameters form a distribution expected from a chance level.

For the population analysis of the coupling properties (Figure 2 and Supplementary Figure 2), we first pulled together the parameter values for each cell pair across all coupled models. We then performed the Wilcoxon rank-sum test to examine the distance and the signal delay between the positively and negatively coupled cells (Figure 2A–F and Supplementary Figure 2A–F). To analyze the symmetry of the coupling effects between cells, we examined by a χ^2-test if the polarity of the signal from one cell to another depends on that in the opposite direction (df=4; Figure 2G–I and Supplementary Figure 2G–I). The data sets from ON and OFF cells were combined as they showed the same trend.

We analyzed in three ways how the coupling affects the behavior of the ganglion cell module (GCM) in the circuit models (Supplementary Figure 4). First, we assessed the input dynamics to GCM as a collective measure of the model's upstream circuit properties. Specifically, for each cell, we compared the outputs of the summation (S) stage in the coupled and non-coupled models (Eq.(S9) in Real et al., 2017) using Pearson's correlation coefficient (Supplementary Figure 4A,D). Second, we examined the GCM feedback filters from the parameters of the second feedback (F) stage in the full models (Eq.(S7) in Real et al. (2017); Supplementary Figure 4B,E). Finally, we compared the GCM nonlinearity parameters (threshold θ and slope α for the second nonlinearity (N) stage; Eq.(S6')) using Pearson's correlation coefficient between the coupled and non-coupled models (Supplementary Figure 4C,F).

Electrophysiology

The dark-adapted retina of a larval tiger salamander (*Ambystoma tigrinum*) or an adult wild-type mouse (*Mus musculus*; C57BL/6J strain) was isolated with an intact optic nerve attached, and placed on a flat array of 61 extracellular electrodes with the ganglion cell side down. The salamander retina was superfused with oxygenated Ringer's medium (in mM: NaCl, 110; $NaHCO_3$, 22; KCl, 2.5; $MgCl_2$, 1.6; $CaCl_2$, 1; and D-glucose, 10; equilibrated with 95% O_2 and 5% CO_2 gas) at room temperature, and the mouse retina with oxygenated Ames' medium (Sigma-Aldrich, A1420) at 37 °C. The electrode array recorded the extracellular signals from ganglion cells with each electrode sampled at 10 kHz, while photoreceptors and/or the optic nerve were stimulated visually and/or electrically, respectively. Spike trains from individual ganglion cells were extracted from raw voltage traces by a semi-automated spike-sorting algorithm (Pouzat et al., 2002) written in IGOR Pro (Wave Metrics).

Glass electrodes filled with the superfusion solution were used to capture the tip of the optic nerve emerging from an isolated retina (Figure 3A). Using custom software written in LabView (National Instruments), we then delivered command signals to a stimulus isolator (Grass Instrument, SD9) for electrically stimulating the optic nerve ending with bipolar pulses (10–50 V, 0.02–0.5 ms) at 2/3–1 Hz (100–200 trials in the dark; 1,300–2,000 trials with visual stimulation). Antidromically evoked spikes were observed in some ganglion cells at a latency of around 5 ms after the nerve stimulation (see for example Figure 3B,C and Supplementary Figure 5A,B). Due to the stimulus artifacts, we were not able to detect any spikes within a few milliseconds after the nerve stimulation (e.g., Figure 3B).

In total, recordings were made from 855 ganglion cells in 19 salamander retinas and 368 cells in 7 mouse retinas for the optic nerve stimulation experiments. Of those, 349 cells in 11 salamander retinas were examined with a gap junction blocker (100 μM meclofenamic acid; Figure 4), 380 cells in 6 salamander retina with inhibitory synaptic transmission blockers (100 μM picrotoxin and 1.0 μM strychnine; Figure 5), and 167 cells in 6 salamander retinas and 172 cells in 3 mouse retinas with visual stimulation. As we focused on a suppression of ganglion cell activity, cells with a sufficiently high baseline firing rate (>1 Hz) were selected for subsequent analyses. Because washout of these drugs from a whole-mount preparation is exceedingly slow,

we could not achieve full reversal of the drug effects within the available time of 30–60 minutes for the stable nerve stimulation. Thus we only compared measurements before and after drug application, with no analysis of the washout.

Visual stimulation

Visual stimuli were displayed on a gamma-corrected cathode-ray tube monitor (DELL E773c; frame rate 100 Hz; mean luminance 18 mW/m^2) and projected onto the photoreceptor layer of the retina from above through a custom-made lens system. We presented full-field random flicker stimuli (100 frames per second; light intensities drawn from Gaussian distribution with mean luminance of 18 mW/m^2 and standard deviation of 7 mW/m^2) for examining the effects of the optic nerve stimulation on the ganglion cell visual responses (Figure 6 and Supplementary Figure 6). Here we could not use spatially-structured stimuli because the stimulation pipette created a distortion in an uncontrollable manner.

Data analysis

Optic nerve stimulation in the dark

To measure the effects of the optic nerve stimulation in the dark (Figures 3–5 and Supplementary Figure 5), we first computed the peri-stimulus time histogram (PSTH) for each ganglion cell with increasing bin sizes (0–10, 10–20, 20–40, 40–80, 80–160, 160–320, and 320–640 ms after the nerve stimulation), and identified those time bins that had significantly different firing rates from the baseline activity (320 ms period before the onset of the nerve stimulation) using bootstrap resampling methods over trials (10,000 repeats). Cells with a significantly increased firing rate in the first time bin (0–10 ms) were considered as the ones directly evoked by the nerve stimulation (Figure 3E and Supplementary Figure 5C, *top* rows) because antidromic spikes typically had a latency of around 5 ms (see Figure 3B,C for example). Cells with significantly different firing rates in the second time bins and thereafter (i.e., $>$10 ms latency) were considered as the ones indirectly affected by the nerve stimulation (Figure 3E and Supplementary Figure 5C, *bottom* rows). For a display purpose, we computed the PSTHs with 20 ms bins in Figure 3C,D and Supplementary Figure 5A,B, and labeled those significantly

below or above the baseline (250 ms period before the onset of the nerve stimulation) in blue and red shades, respectively.

Optic nerve stimulation with visual stimulation

We used stimulus ensemble statistical techniques ("reverse correlation" methods; 400 ms window; 10 ms bin width) to calculate the linear filter and static nonlinear gain function of the recorded cells (Figure 6 and Supplementary Figure 6). Specifically, for each ganglion cell, we first computed the PSTH (100 ms bin width) with respect to the nerve stimulation during the full-field random flicker stimulus presentation, and identified those time bins with significantly higher or lower firing rates than the baseline (500 ms period before the nerve stimulation) using the bootstrap resampling methods over trials (10,000 repeats; e.g., Figure 6B and Supplementary Figure 6A). For each time bin, we then estimated the linear filter by a spike-triggered average stimulus (e.g., Figure 6C and Supplementary Figure 6B). The obtained linear filters indicate the average stimulus features that made the cell fire action potentials. We then characterized the change in their profile from the baseline using the ON-OFF index, defined as the difference between the peak and valley values of the linear filter, normalized by the sum of the two:

$$\text{ON-OFF index} = \frac{|\text{peak}| - |\text{valley}|}{|\text{peak}| + |\text{valley}|}. \tag{4}$$

The ON-OFF index value of -1, 1, and 0 indicates the stimulus feature selectivity towards purely OFF stimuli, purely ON stimuli, and both ON and OFF stimuli, respectively (e.g., Figure 6C and Supplementary Figure 6B). Sign-test was used to evaluate the linear filter profile change over the population during the suppressed and enhanced firing periods, and F-test was used to compare the variance between them (Figure 6E and Supplementary Figure 6D).

For each epoch, we also computed the static nonlinear gain function $P(\text{response}|\text{stimulus})$ as a function of the linear filter output values by the convolution with stimulus fragments:

$$P(\text{response}|\text{stimulus}) = \frac{N(\text{stimulus}|\text{response})}{N(\text{stimulus})}, \tag{5}$$

where $N(\text{stimulus})$ and $N(\text{stimulus}|\text{response})$ are the distributions obtained from all stimuli and spike-triggered stimulus ensembles, respectively (Figure 6D and Supplementary Figure 6C, *bottom* panels). For quantification, we fitted the following sigmoid function $f(x)$ to the gain function profiles:

$$f(x) = \frac{u - l}{1 + \exp[-s(x - c)]} + l, \tag{6}$$

and calculated the change in the parameters (u, upper bound; l, lower bound; c, center; s, slope) from the baseline (e.g., Figure 6D and Supplementary Figure 6C). Sign-test and F-test were performed to test the statistical significance (Figure 6F,G and Supplementary Figure 6E,F).

Figure legends

Figure 1: Coupling model outperforms non-coupling model.

(A) Schematic diagram of the circuit model with couplings among retinal ganglion cells ("LNSCN" model; see also Supplementary Figure 1). The target ganglion cell (red) integrates inputs from upstream bipolar cells as well as surrounding retinal ganglion cells (blue) with certain coupling strengths and delays. The model without couplings is identical to the "LNSN" model in Real et al. (2017).

(B) Receptive field centers of 20 OFF ganglion cells simultaneously recorded from an isolated salamander retina (red, representative modelled cell in C and D; blue, cells included in the coupling model for the representative cell; gray, cells excluded from the coupling model due to high spike correlations with the modelled cell; see also Supplementary Figure 3A). Each outline represents a two-dimensional Gaussian fit to the receptive field profile (contour at 1 standard deviation).

(C) Responses of ganglion cells (red, representative modelled cell from B; blue, cells included in the coupling model) to repetitions of the white noise stimulus (8 repeats in total). Each row in the raster denotes spikes from a single stimulus repeat for each cell. Cyan lines indicate

timepoints where false positive responses in the non-coupled LNSN model were suppressed in the coupled LNSCN model (arrows in D).

(D) Time course of the firing rate of the representative cell (red) and that of the model outputs with (black, LNSCN model) and without (cyan, LNSN model) couplings fitted to this cell. The LNSN model occasionally mis-predicted responses at which the cell did not fire spikes, but the LNSCN model correctly suppressed them in many cases (arrows). The coupling parameters (coupling strength and delay) for each surrounding cell included in the LNSCN model are shown next to the raster graph in C.

(E) LNSCN model performance gain over LNSN model for salamander ganglion cells, calculated as a difference of the coefficients of determination (R^2, Eq.(3) in Methods; see also Supplementary Figure 1B). Each data point represents a cell (left, N=185 OFF cells with OFF neighbors; right, N=35 OFF cells with ON neighbors and 4 ON cells with OFF neighbors; red circle, representative cell in B–D). The LNSCN model outperforms the LNSN model more strongly with the neighboring cells of the same response polarity (left; ΔR^2=1.7±1.6, mean ± standard deviation; p<0.001, paired t-test) than with those of different polarities (right; ΔR^2=1.3±1.7; p<0.001). Here and thereafter, three stars ($\star\star\star$) indicate p<0.001; $\star\star$, p<0.01; and $\star$, p<0.05.

(F) Corresponding figure panel for the mouse ganglion cells (see also Supplementary Figure 1C). The LNSCN model outperforms the LNSN model when the neighboring cells of the same response polarity are included (left, N=10 ON cells with ON neighbors and 12 OFF cells with OFF neighbors; ΔR^2=0.7±0.7; p<0.001), but not with the neighboring cells of different polarities (right, N=10 ON cells with OFF neighbors and 12 OFF cells with ON neighbors; ΔR^2=0.1±1.0; p>0.5).

Figure 2: Coupling model predicts faster enhancing effects among proximal retinal ganglion cells and slower suppressing effects among distal cells.

(A, B) Coupling strength (A) and delay (B) parameter values from the LNSCN model plotted as a function of the distance between salamander retinal ganglion cells of the same response polarity (1460 OFF cell pairs in total; yellow circles, representative cases in Figure 1B–D). The noise level was determined by shuffling analysis (gray, 0.5 and 99.5 percentile; see Methods for details). Positive couplings (red, N=211) were found at a shorter distance (A; 0.31±0.14 versus 0.40±0.26 mm; median±interquartile range as shown by the box plot; p<0.001, rank-sum test) with a shorter latency (B; 0.35±3.6 ms versus 4.6±4.0 ms; p<0.001) than negative couplings (blue, N=98).

(C, D) Corresponding figure panels for salamander cells with different response polarities (47 OFF cells with ON neighbors and 46 ON cells with OFF neighbors in total). Couplings above the noise level were mostly positive (N=10) with the distance of 0.28±0.08 mm (C; median±interquartile range) and the latency of 4.2±1.5 ms (D).

(E, F) Corresponding figure panels for mouse retinal ganglion cells of the same response polarity (76 ON cell pairs and 116 OFF cell pairs in total). Positive couplings (red, 18 ON and 15 OFF cell pairs) were found at a shorter distance (C; 0.33±0.25 mm versus 0.78±0.74 mm; p=0.002) and with a shorter latency (D; 0.0±0.0 versus 21.9±13.8 ms; p<0.001) than negative couplings (blue, 7 ON and 9 OFF cell pairs). Data not analyzed for the mouse cells with different response polarities because the coupled model performance did not show an improvement (Figure 1F).

(G–I) Comparison of the coupling strengths from one cell to another and vice versa (black, couplings above the noise level in both directions; dark grey, above the noise level only in one direction; light gray, both below the noise level). The number of data points in each category is shown in the figure panels. Symmetric, either mutually positive or negative, couplings were found more frequently than expected in both salamander (G, between cells of the same response

polarity; H, between cells with different response polarities) and mouse (I, between cells of the same response polarity) retinas ($p<0.001$ in all three cases, χ^2-test with $df=4$)

Figure 3: Optic nerve stimulation produces fast excitation and slow inhibition in retinal ganglion cell firing activity.

(A) Schematic diagram of the experiment. The tip of the optic nerve emerging from an isolated retina was electrically stimulated with a glass pipette (inter-stimulus interval, 1–1.5 s), while a population of ganglion cells was simultaneously recorded with a multi-electrode array (see B for example). A, amacrine cell; G, ganglion cell; open circle, inhibitory synapse; resistor symbol, electrical synapse. The other retinal cell types and synapses are omitted for simplification.

(B) Example raw data traces from an isolated salamander retina overlaid across trials of the optic nerve stimulation in the dark. The lightning symbol indicates the stimulation onset, and the gray area indicates the window for which the magnified traces are shown at the bottom panel. The antidromic spikes are indicated by the asterisk.

(C, D) Representative responses of retinal ganglion cells to the optic nerve stimulation (top, raster graphs; bottom, peri-stimulus time histogram (PSTH), magnified at the bottom for the window indicated by the gray area). A period of suppression was observed in cells either with (C) or without (D) antidromically evoked spikes (asterisk). Red- and blue-shaded bins in the PSTHs indicate those in which the firing rate significantly increased or decreased from the spontaneous activity, respectively.

(E) Population data of the ganglion cell responses to the nerve stimulation (top row, cells with antidromic spikes; bottom row, cells without antidromic spikes), classified into four different groups: no indirect effect, enhancement, suppression, or both effects after the nerve stimulation (from left to right columns). Each gray line represents the evoked firing rate of a cell, and the black line shows the mean over the cells in each group. Red and blue circles indicate the time bins in which the firing rate was significantly higher or lower than the spontaneous activity, respectively. The representative cells in B and C are shown in magenta.

Figure 4: Negative feedback involves electrical synapses.

(A) Spiking activity of a salamander retinal ganglion cell in the dark (top, raster graphs; bottom, PSTHs) in response to the optic nerve stimulation in the absence (black; control) and presence (brown) of gap junction blockers (100 μM meclofenamic acid; MFA). The suppression after the nerve stimulation was abolished after blocking electrical synapses.

(B) Summary of the effects of blocking gap junctions on the ganglion cell firing patterns after the nerve stimulation (top, control; bottom, with MFA), shown in the same format as Figure 3D (magenta, the representative cell in A). The suppression after the nerve stimulation was abolished after blocking electrical synapses (right: 7 out of 8 cells; p=0.036, Fisher's exact test), whereas the enhancement remained (left; 11 out of 11 cells).

Figure 5: Negative feedback requires inhibitory synaptic transmission.

(A) Spiking activity of a salamander retinal ganglion cell (top, raster graph; bottom, PSTHs) in response to the optic nerve stimulation in the absence (black; control) and presence (green) of inhibitory synaptic transmission blockers (100 μM picrotoxin and 1.0 μM strychnine; PTX+STR). The suppression after the nerve stimulation was abolished after blocking inhibitory transmission.

(B) Summary of the effects of blocking inhibitory synaptic transmission on the ganglion cell firing patterns after the nerve stimulation (top, control; bottom, with PTX+STR), shown in the same format as Figure 3D (magenta, the representative cell in A) The suppression after the nerve stimulation was abolished after blocking inhibitory transmission (right: 7 out of 7 cells; p=0.008, Fisher's exact test), whereas the enhancement remained (left; 11 out of 11 cells).

Figure 6: Negative feedback modulates the visual response gain but not the feature selectivity.

(A) Schematic diagram of the experiment and analysis. Full-field white-noise visual stimuli were presented together with the optic nerve stimulation (inter-stimulus intervals, 1–1.5 s) to

probe changes in the LN model parameters at different time windows from the nerve stimulation (see B–D for example). The linear filter represents the stimulus feature selectivity of a cell, while the static nonlinearity indicates the visual response gain.

(B) PSTH of a representative salamander ganglion cell with respect to the optic nerve stimulation during the visual stimulus presentation. Blue-shaded bins (0–100 ms after the nerve shock) indicate those in which the firing rate was significantly lower than the baseline response of the cell (500 ms before the nerve stimulation).

(C) *Left*: Linear filters of the example cell obtained by the reverse-correlation methods (i.e., spike-triggered average stimulus) using the spikes in different time bins from the PSTH (blue, 0–100 ms bin with significantly lower firing rates from B; gray, all the other 100 ms bins without significant firing rate changes; black, baseline). *Right*: Dynamics of the linear filter profile with respect to the time from the nerve shock, quantified by an ON-OFF index (i.e., the difference between the peak and valley values divided by the sum of the two; Eq.(4) in Methods).

(D) *Left*: Static nonlinearity of the example cell, computed for each corresponding linear filter at different time bins (Eq.(5) in Methods). A sigmoid function (Eq.(6) in Methods) was fitted to quantify the nonlinear profile (e.g., light blue for the suppressed period at 0–100 ms after the nerve shock, with the upper and lower bounds of the cell's firing probability in dotted horizontal lines). *Right*: The upper and lower bound dynamics of the example cell's firing probability with respect to the time from the nerve shock. The cell's response gain (upper bound) became lower during the period of suppressed firing, while the stimulus feature selectivity remained unchanged (ON-OFF index in C, right).

(E) Summary of the changes in the ON-OFF indices between the periods with and without significant firing rate changes after the nerve stimulation (blue, decrease N=25; red, increase N=94; magenta, the representative cells in A). The horizontal and vertical lines represent the mean and standard deviation, respectively. The linear filter profile was more strongly modulated during the enhanced firing period than the suppressed firing period (p=0.03, F-test). Because

the modulation can be in either polarity, however, on average there was no significant difference from the baseline (p>0.3 for both cases, sign-test).

(F,G) Summary of the changes in the sigmoid function parameters fitted to the nonlinearity. The upper bounds (F) were significantly decreased during the suppressed firing periods (blue, p<0.001, sign-test), but not affected during the enhanced firing periods (red, p=0.08) despite a larger variability (p<0.001, F-test). In contrast, the lower bounds (G) were significantly increased during the enhanced firing period (p<0.001) but not affected during the suppressed firing period (p>0.5). The other parameters (center and slope) did not change significantly (not shown).

Supplementary Figure Legends

Supplementary Figure 1: Retinal ganglion cell couplings improve the performance of the full circuit model.

(A) Schematic diagram of the full circuit model with couplings ("LNFDSCNF" model). The model without couplings is identical to the "LNFDSNF" model in Real et al. (2017).

(B, C) LNFDSCNF model performance gain over LNFDSNF model for salamander (B; left, ΔR^2=0.83±0.83, p<0.001, for coupled cells with the same response polarity; right, ΔR^2=0.55±0.74, p<0.001, for those with different polarities; mean ± standard deviation, paired t-test) and mouse (C; left, ΔR^2=0.42±0.21, p<0.001; right, ΔR^2=0.01±0.07, p=0.4) retinal ganglion cells. The figure panels are displayed in the same format as Figure 1E.

Supplementary Figure 2: The circuit model predictions hold with the full circuit model.

The data are shown in the same format as Figure 2 but for the LNFDSCNF model.

(A, B) Coupling strength (A) and delay (B) parameter values plotted as a function of the distance between salamander retinal ganglion cells of the same response polarity. As is the case with the LNSCN model (Figure 2), positive couplings (red, N=154) were found at a shorter distance (A; 0.31±0.14 mm versus 0.36±0.20 mm; median ± interquartile range (box plot); p<0.001, rank-sum test) and with a shorter latency (B; 2.3±4.7 versus 4.7±5.2 ms; p<0.001) than negative couplings (blue, N=64).

(C, D) Corresponding figure panels for salamander cells with different response polarities. Couplings above the noise level were all positive (N=11) with the distance of 0.29±0.06 mm (C; median ± interquartile range) and the latency of 3.8±6.5 ms (D).

(E, F) Corresponding figure panels for mouse retinal ganglion cells of the same response polarity. Likewise, positive couplings (red, N=37) were found at a shorter distance (C; 0.35±0.28 mm versus 0.72±0.65 mm; p=0.02) and with a shorter latency (D; 0.00±0.04 ms versus 19.1±7.7 ms; p<0.001) than negative couplings (blue, N = 6). Data not analyzed for the mouse cells with different response polarities because the coupled model performance did not improve significantly (Supplementary Figure 1C).

(G–I) Comparison of the coupling strengths from one cell to another and vise versa. Ganglion cells have symmetric couplings more frequently than expected in both salamander (G, p<0.001, χ^2-test with df=4, between cells of the same response polarity; H, p<0.001, between cells with different response polarities) and mouse (I; p<0.001, between cells of the same response polarity) retinas. The number of data points in each category is shown in the figure panels.

Supplementary Figure 3: Ganglion cell pairs with low spike correlations can have strong couplings in either polarity.

(A) Pairwise spike correlations of the representative cell (#25 from Figure 1B–D; auto-correlation) and all the other simultaneously recorded 19 cells (cross-correlations). Those cells with too high correlations (gray; ≥0.1 or ≤−0.1 at the peak) were excluded from our model analysis to minimize the confounding effects of common visual inputs (see Methods for details).

The coupling strength is shown on the top right for each cell included in the LNSCN model for the cell #25 (black).

(B, C) Coupling strength from the LNSCN model as a function of the Pearson cross-correlation of firing patterns between ganglion cell pairs (B, salamander; C, mouse). Although we selected only those cells with low spike correlations (from -0.1 to 0.1) in the coupling models, we frequently found strong couplings in either polarity. The cells in the representative data set (from A) are highlighted with yellow circles.

(D, E) Corresponding figure panels for the LNFDSCNF model.

Supplementary Figure 4: Ganglion cell module properties do not differ between the coupled and non-coupled models.

(A) Distribution of the ganglion cell module (GCM) input correlation between coupled and non-coupled models fitted to salamander cells (black, reduced models: LNSCN versus LNSN, 0.987 ± 0.020, median $\pm$ interquartile range; gray, full models: LNFDSCNF versus LNFDSNF, 0.996 ± 0.005). The correlation was calculated using the outputs of the summation (S) stage in the models (Eq.(S9) in Real et al., 2017). High correlations indicate that the GCM input dynamics are nearly identical in response to the visual stimuli (arrow, representative cell in Figure 1B–D).

(B) The second feedback (F) stage (GCM feedback filters; Eq.(S7) in Real et al., 2017) was nearly identical between the non-coupled (left, LNFDSNF) and the coupled (right, LNFDSCNF) models (yellow, representative cell in Figure 1B–D; gray, all the other cells; red, mean).

(C) Comparison of the second nonlinear (N) stage (GCM nonlinearity) between the coupled and non-coupled models (top, LNSN versus LNSCN; bottom, LNFDSNF versus LNFDSCNF; yellow, representative cell in Figure 1B–D. Couplings did not affect the slope (left, α in

Eq.(S6'); Pearson's R=0.979 and 0.997 for the reduced and full models, respectively) or the threshold (right, θ in Eq.(S6'); R=0.955 and 0.997, respectively).

(D–F) Corresponding figure panels for mouse retinal ganglion cells. There was no marked difference between the coupled and non-coupled models in GCM input correlations (D; black, reduced models, 0.994±0.005; gray, full models, 0.998±0.003), GCM feedback (E), GCM slope (F, left; R=0.967 and 0.978 for the reduced (top) and full (bottom) models, respectively) or GCM slope (F, right; R=0.991 and 0.996, respectively).

Supplementary Figure 5: Optic nerve stimulation produces fast excitation and slow inhibition in ganglion cell firing activity in an isolated mouse retina.

The data are shown in the same format as Figure 3 but for the mouse retina.

(A, B) Firing patterns of two representative retinal ganglion cells, showing a period of suppression after the optic nerve stimulation (asterisk, antidromically evoked spikes) in the dark. Note the cell in B showed a period of enhanced firing before the suppression, while the one in A did not.

(C) Population data of the ganglion cell responses to the nerve stimulation (top row, cells with antidromic spikes; bottom row, cells without antidromic spikes), classified into four different groups: no indirect effect, enhancement (red circles, significant increase), suppression (blue circles, significant decrease), or both effects after the nerve stimulation (from left to right columns).

Supplementary Figure 6: Negative feedback modulates the visual response properties of mouse retinal ganglion cells.

The data are shown in the same format as Figure 6 but for the mouse retina.

(A) PSTH of a representative mouse ganglion cell with respect to the optic nerve stimulation during the visual stimulus presentation. Blue- and red-shaded bins indicate those with significantly higher and lower firing rates than the baseline, respectively.

(B) Linear filters of the example cell (left) and corresponding ON-OFF indices (right; Eq.(4) in Methods) at different time bins from the nerve stimulation. The filter became more biphasic during which the visual responses were enhanced by the nerve stimulation (red, 0–100 ms bin with significantly higher firing rates), but it went back to normal even when the visual responses were suppressed (blue, 200–300 ms bin with significantly lower firing rates; gray, all the other 100 ms bins, with the mean in black).

(C) Static nonlinearities of the example cell (left; Eq.(5) in Methods) and the upper and lower bounds of the cell's firing probability from sigmoidal curve fits (right; Eq.(6) in Methods) at different time bins from the nerve stimulation. The upper bound was lower during the suppressed firing period (blue, 200–300 ms bin) while the lower bound was higher during the enhanced firing period (red, 0–100 ms bin) compared to the control period (gray, all the other 100 ms bins; black, mean).

(D) Summary of the changes in the ON-OFF indices between the periods with and without significant firing rate changes after the nerve stimulation (blue, decrease N=4; red, increase N=17; magenta, example cell in A).

(E,F) Summary of the changes in the sigmoid function parameters fitted to the nonlinearity (E, upper bounds; F, lower bounds; center and slope, not shown; magenta, example cell in A).

References

Asari, H. and Meister, M. (2012). Divergence of visual channels in the inner retina. Nat Neurosci, 15, 1581–1589.

Asari, H. and Meister, M. (2014). The projective field of retinal bipolar cells and its modulation by visual context. Neuron, 81, 641–652.

Baden, T., Berens, P., Franke, K., Román Rosón, M., Bethge, M., and Euler, T. (2016). The functional diversity of retinal ganglion cells in the mouse. Nature, 529, 345–350.

Berry, M. J., Brivanlou, I. H., Jordan, T. A., and Meister, M. (1999). Anticipation of moving stimuli by the retina. Nature, 398, 334–338.

Bloomfield, S. A. and Völgyi, B. (2009). The diverse functional roles and regulation of neuronal gap junctions in the retina. Nat Rev Neurosci, 10, 495–506.

Brivanlou, I. H., Warland, D. K., and Meister, M. (1998). Mechanisms of concerted firing among retinal ganglion cells. Neuron, 20, 527–539.

Carandini, M. and Heeger, D. J. (2012). Normalization as a canonical neural computation. Nat Rev Neurosci, 13, 51–62.

Chen, X., Hsueh, H.-A., Greenberg, K., and Werblin, F. S. (2010). Three forms of spatial temporal feedforward inhibition are common to different ganglion cell types in rabbit retina. J Neurophysiol, 103, 2618–2632.

Chichilnisky, E. J. (2001). A simple white noise analysis of neuronal light responses. Network, 12, 199–213.

Cocco, S., Leibler, S., and Monassond, R. (2009). Neuronal couplings between retinal ganglion cells inferred by efficient inverse statistical physics methods. Proc Natl Acad Sci U S A, 106, 14058–14062.

Cook, J. E. and Becker, D. L. (1995). Gap junctions in the vertebrate retina. Microsc Res Tech, 31, 408–419.

Cooler, S. and Schwartz, G. W. (2020). An offset on-off receptive field is created by gap junctions between distinct types of retinal ganglion cells. bioRxiv, 2020.07.15.205336.

Dong, C. J. and Werblin, F. S. (1998). Temporal contrast enhancement via $GABA_c$ feedback at bipolar terminals in the tiger salamander retina. J Neurophysiol, 79, 2171–2180.

Euler, T., Haverkamp, S., Schubert, T., and Baden, T. (2014). Retinal bipolar cells: elementary building blocks of vision. Nat Rev Neurosci, 15, 507–519.

Franke, K., Berens, P., Schubert, T., Bethge, M., Euler, T., and Baden, T. (2017). Inhibition decorrelates visual feature representations in the inner retina. Nature, 542, 439–444.

Gastinger, M. J., Tian, N., Horvath, T., and Marshak, D. W. (2006). Retinopetal axons in mammals: Emphasis on histamine and serotonin. Curr Eye Res, 31, 655–667.

Geffen, M. N., de Vries, S. E. J., and Meister, M. (2007). Retinal ganglion cells can rapidly change polarity from Off to On. PLoS Biol, 5, e65.

Gollisch, T. and Meister, M. (2008). Rapid neural coding in the retina with relative spike latencies. Science, 319, 1108–1111.

Gollisch, T. and Meister, M. (2010). Eye smarter than scientists believed: Neural computations in circuits of the retina. Neuron, 65, 150–164.

Gouras, P. (1969). Antidromic responses of orthodromically identified ganglion cells in monkey retina. J Physiol, 204, 407–419.

Greschner, M., Heitman, A. K., Field, G. D., Li, P. H., Ahn, D., Sher, A., Litke, A. M., and Chichilnisky, E. J. (2016). Identification of a retinal circuit for recurrent suppression using indirect electrical imaging. Curr Biol, 26, 1935–1942.

Herz, A. V. M., Gollisch, T., Machens, C. K., and Jaeger, D. (2006). Modeling single-neuron dynamics and computations: a balance of detail and abstraction. Science, 314, 80–85.

Ito, M. (2000). Mechanisms of motor learning in the cerebellum. Brain Res, 886, 237–245.

Kenyon, G. T. and Marshak, D. W. (1998). Gap junctions with amacrine cells provide a feedback pathway for ganglion cells within the retina. Proc Biol Sci, 265, 919–925.

Koves, K., Csaki, A., and Vereczki, V. (2016). Recent research on the centrifugal visual system in mammalian species. Anat Physiol, 6, 3.

Lefebvre, J. L., Zhang, Y., Meister, M., Wang, X., and Sanes, J. R. (2008). Gamma-protocadherins regulate neuronal survival but are dispensable for circuit formation in retina. Development, 135, 4141–4151.

Maass, W. and Markram, H. (2002). On the computational power of recurrent circuits of spiking neurons. J Comput Syst Sci, 69, 593–616.

Masland, R. H. (2012). The neuronal organization of the retina. Neuron, 76, 266–280.

Mastronarde, D. N. (1983). Interactions between ganglion cells in cat retina. J Neurophysiol, 49, 350–365.

Matthews, G. (1999). Synaptic mechanisms of bipolar cell terminals. Vision Res, 39, 2469–2476.

Meister, M., Lagnado, L., and Baylor, D. A. (1995). Concerted signaling by retinal ganglion cells. Science, 270, 1207–1210.

Nirenberg, S. and Meister, M. (1997). The light response of retinal ganglion cells is truncated by a displaced amacrine circuit. Neuron, 18, 637–650.

Pereda, A. E., Curti, S., Hoge, G., Cachope, R., Flores, C. E., and Rash, J. E. (2013). Gap junction-mediated electrical transmission: regulatory mechanisms and plasticity. Biochim Biophys Acta, 1828, 134–146.

Pillow, J. W., Shlens, J., Paninski, L., Sher, A., Litke, A. M., Chichilnisky, E. J., and Simoncelli, E. P. (2008). Spatio-temporal correlations and visual signalling in a complete neuronal population. Nature, 454, 995–999.

Pouzat, C., Mazor, O., and Laurent, G. (2002). Using noise signature to optimize spike-sorting and to assess neuronal classification quality. J Neurosci Methods, 122, 43–57.

Real, E., Asari, H., Gollisch, T., and Meister, M. (2017). Neural circuit inference from function to structure. Curr Biol, 27, 189–198.

Repérant, J., Ward, R., Miceli, D., Rio, J. P., Médina, M., Kenigfest, N. B., and Vesselkin, N. P. (2006). The centrifugal visual system of vertebrates: a comparative analysis of its functional anatomical organization. Brain research reviews, 52, 1–57.

Roska, B., Molnar, A., and Werblin, F. S. (2006). Parallel processing in retinal ganglion cells: how integration of space-time patterns of excitation and inhibition form the spiking output. J Neurophysiol, 95, 3810–3822.

Roska, B., Nemeth, E., Orzo, L., and Werblin, F. S. (2000). Three levels of lateral inhibition: A space-time study of the retina of the tiger salamander. J Neurosci, 20, 1941–1951.

Roy, S. and Field, G. D. (2019). Dopaminergic modulation of retinal processing from starlight to sunlight. J Pharmacol Sci, 140, 86–93.

Sakai, H. M. and Naka, K. I. (1988). Dissection of the neuron network in the catfish inner retina. II. Interactions between ganglion cells. J Neurophysiol, 60, 1568–1583.

Sakai, H. M. and Naka, K. I. (1990). Dissection of the neuron network in the catfish inner retina. IV. bidirectional interactions between amacrine and ganglion cells. J Neurophysiol, 63, 105–119.

Tachibana, M. and Kaneko, A. (1988). Retinal bipolar cells receive negative feedback input from GABAergic amacrine cells. Vis Neurosci, 1, 297–305.

Trong, P. K. and Rieke, F. (2008). Origin of correlated activity between parasol retinal ganglion cells. Nat Neurosci, 11, 1343–1351.

Van Rullen, R. and Thorpe, S. J. (2001). Rate coding versus temporal order coding: What the retinal ganglion cells tell the visual cortex. Network: Comput Neural Syst, 13, 1255–1283.

Victor, J. D. (1999). Temporal aspects of neural coding in the retina and lateral geniculate. Network: Comput Neural Syst, 10, R1–R66.

Völgyi, B., Chheda, S., and Bloomfield, S. A. (2009). Tracer coupling patterns of the ganglion cell subtypes in the mouse retina. J Comp Neurol, 512, 664–687.

Völgyi, B., Pan, F., Paul, D. L., Wang, J. T., Huberman, A. D., and Bloomfield, S. A. (2013). Gap junctions are essential for generating the correlated spike activity of neighboring retinal ganglion cells. PloS one, 8, e69426.

Wang, X.-J. (2008). Decision making in recurrent neuronal circuits. Neuron, 60, 215–234.

Wark, B., Fairhall, A., and Rieke, F. (2009). Timescales of inference in visual adaptation. Neuron, 61, 750–761.

Wässle, H. (2004). Parallel processing in the mammalian retina. Nat Rev Neurosci, 5, 747–757.

Werblin, F. S. (2011). The retinal hypercircuit: a repeating synaptic interactive motif underlying visual function. J Physiol, 589, 3691–3702.

Witkovsky, P. and Dearry, A. (1991). Functional roles of dopamine in the vertebrate retina. Prog Retinal Res, 11, 247–292.

Wu, M. C.-K., David, S. V., and Gallant, J. L. (2006). Complete functional characterization of sensory neurons by system identification. Annu Rev Neurosci, 29, 477–505.

Zhang, A.-J. and Wu, S. M. (2009). Receptive fields of retinal bipolar cells are mediated by heterogeneous synaptic circuitry. J Neurosci, 29, 789–797.

Zhang, A.-J. and Wu, S. M. (2010). Responses and receptive fields of amacrine cells and ganglion cells in the salamander retina. Vision Res, 50, 614–622.

Zhang, D.-Q., Belenky, M. A., Sollars, P. J., Pickard, G. E., and McMahon, D. G. (2012). Melanopsin mediates retrograde visual signaling in the retina. PloS one, 7, e42647.

Zhang, D.-Q., Wong, K. Y., Sollars, P. J., Berson, D. M., Pickard, G. E., and McMahon, D. G. (2008). Intraretinal signaling by ganglion cell photoreceptors to dopaminergic amacrine

neurons. Proceedings of the National Academy of Sciences of the United States of America, 105, 14181–14186.

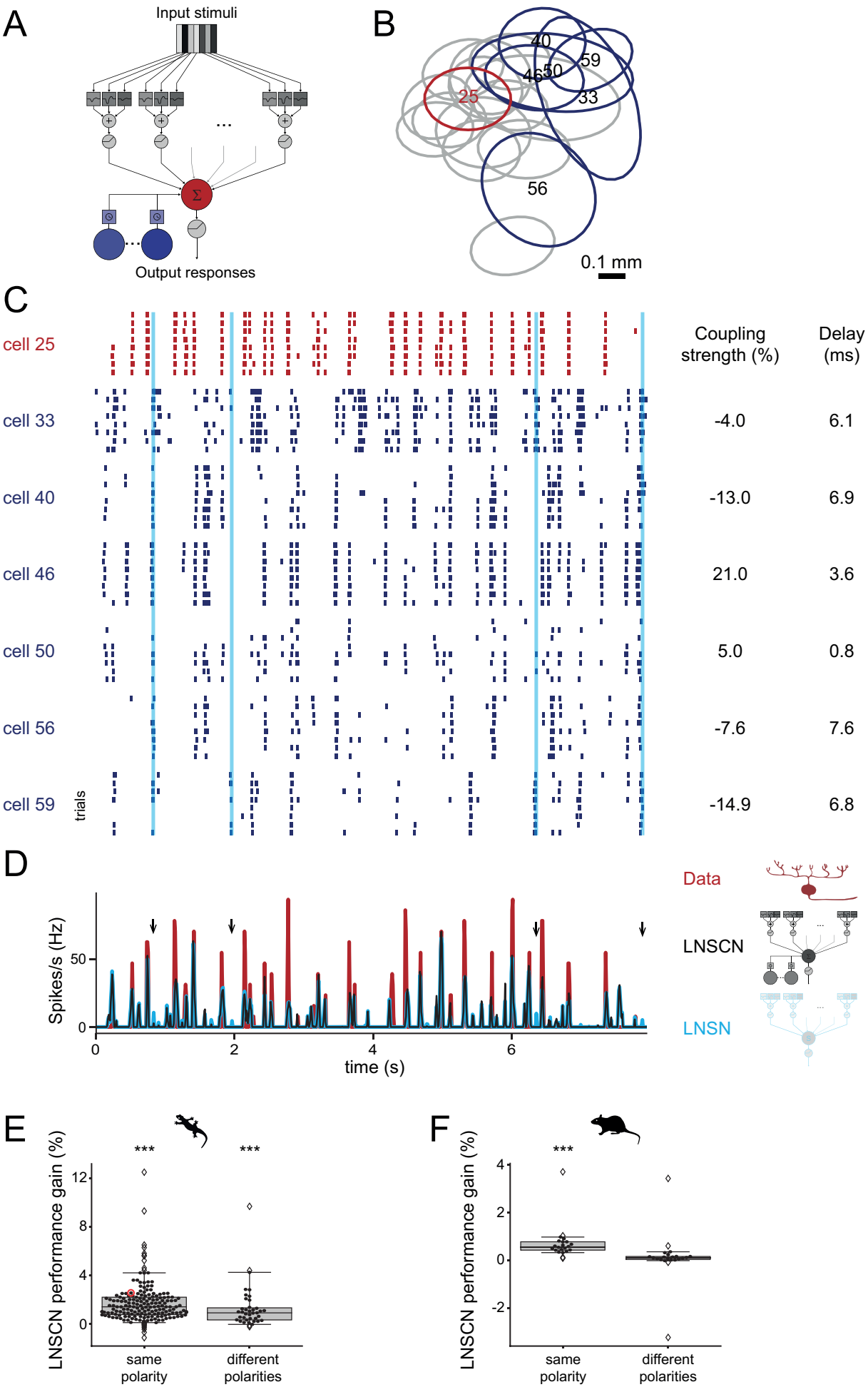
A
Input stimuli
Output responses
B
40
59
46
50
25
33
56
0.1 mm
C
cell 25
cell 33
cell 40
cell 46
cell 50
cell 56
cell 59
trials
Coupling strength (%)
Delay (ms)
-4.0
6.1
-13.0
6.9
21.0
3.6
5.0
0.8
-7.6
7.6
-14.9
6.8
D
Spikes/s (Hz)
50
0
0
2
4
6
time (s)
Data
LNSCN
LNSN
E
LNSCN performance gain (%)
12
8
4
0
***
***
same polarity
different polarities
F
LNSCN performance gain (%)
4
2
0
-2
***
same polarity
different polarities

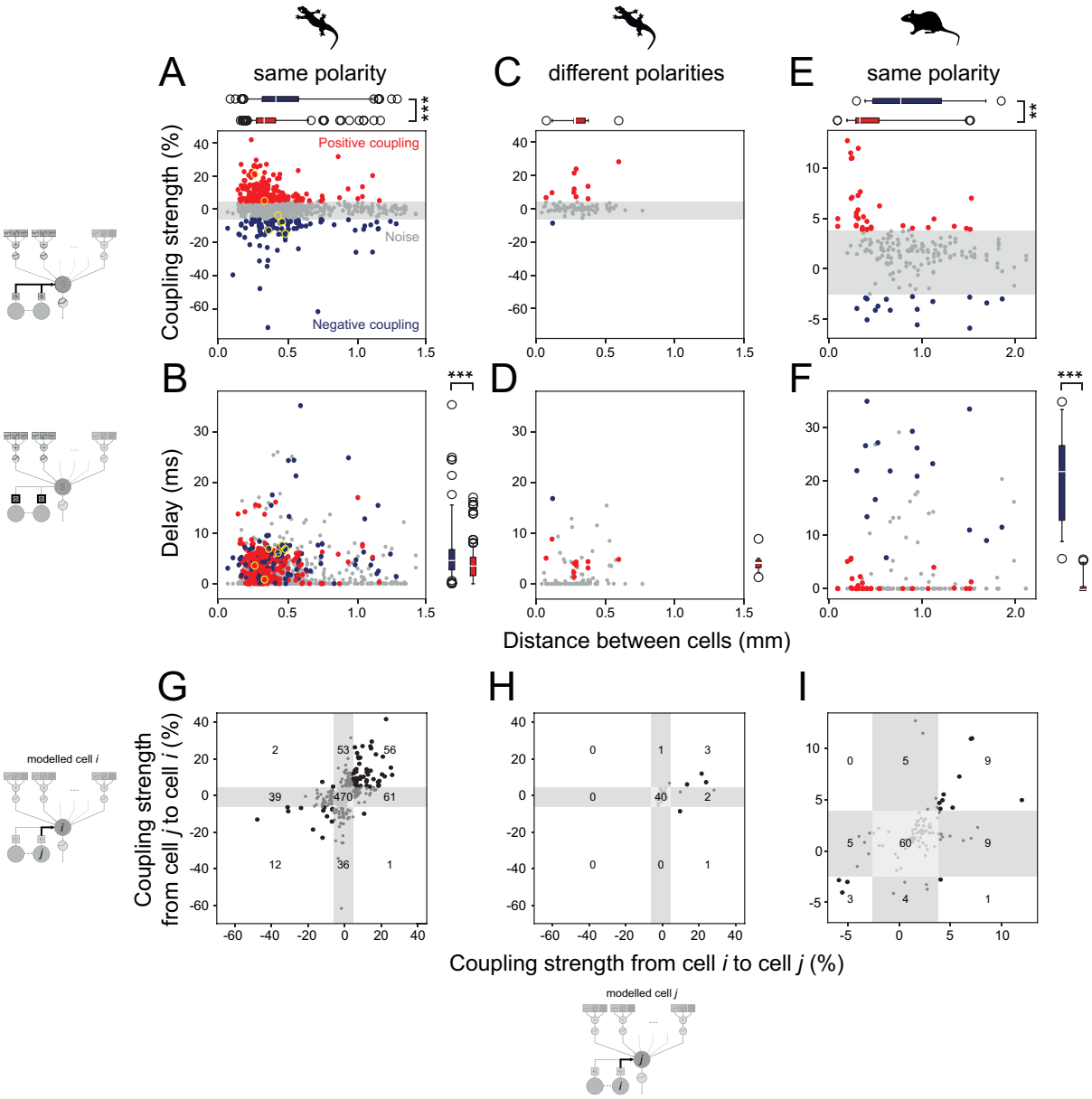
A
same polarity
C
different polarities
E
same polarity
Positive coupling
Noise
Negative coupling
Coupling strength (%)
B
D
F
Delay (ms)
Distance between cells (mm)
G
H
I
modelled cell i
Coupling strength from cell j to cell i (%)
Coupling strength from cell i to cell j (%)
modelled cell j

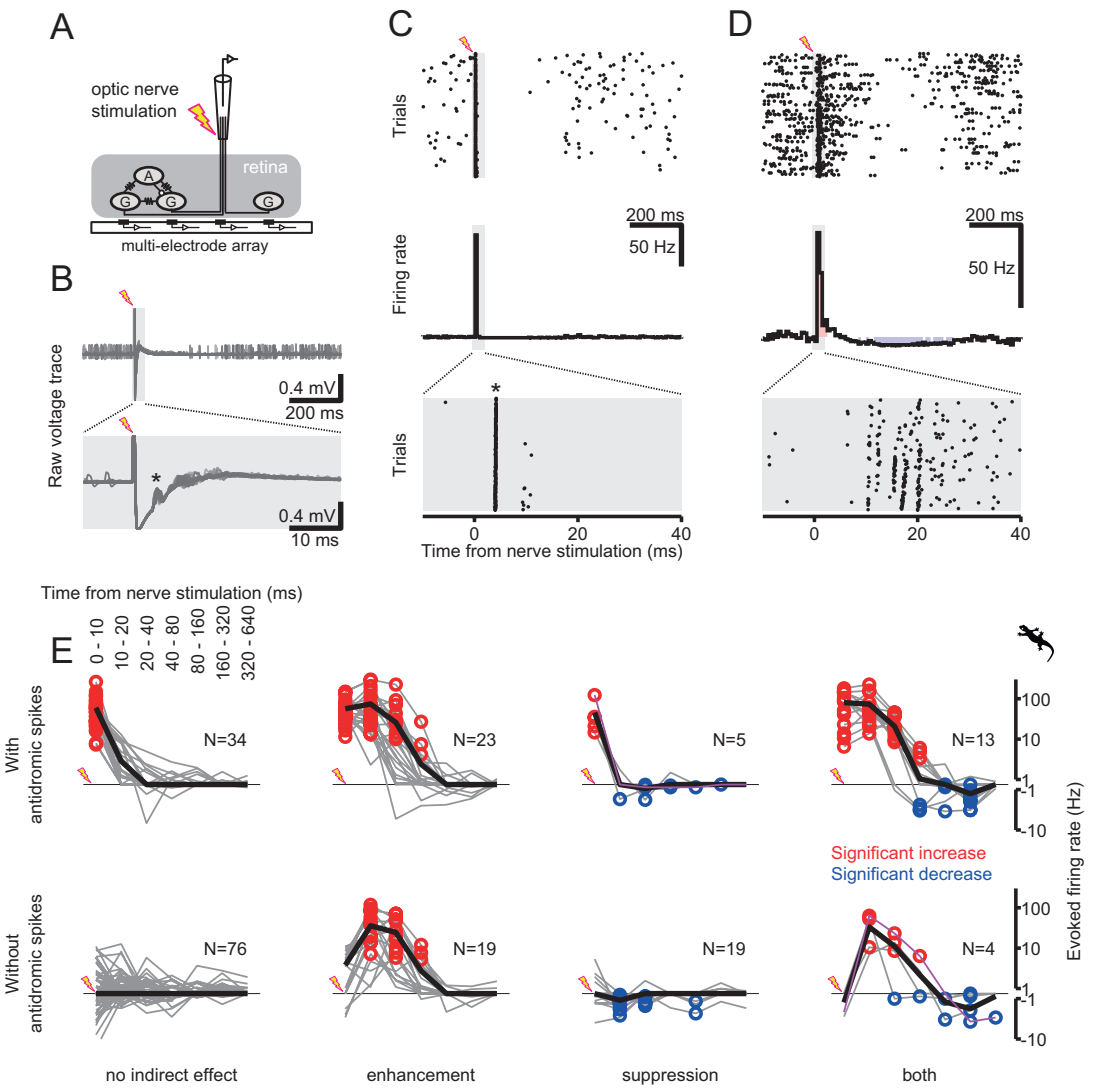
A
optic nerve stimulation
retina
A
G
G
G
multi-electrode array
B
Raw voltage trace
0.4 mV
200 ms
0.4 mV
10 ms
C
Trials
Firing rate
200 ms
50 Hz
Trials
0
20
40
Time from nerve stimulation (ms)
D
200 ms
50 Hz
0
20
40
Time from nerve stimulation (ms)
E
0 - 10
10 - 20
20 - 40
40 - 80
80 - 160
160 - 320
320 - 640
With antidromic spikes
Without antidromic spikes
N=34
N=23
N=5
N=13
N=76
N=19
N=19
N=4
100
10
1
-1
-10
Significant increase
Significant decrease
Evoked firing rate (Hz)
no indirect effect
enhancement
suppression
both

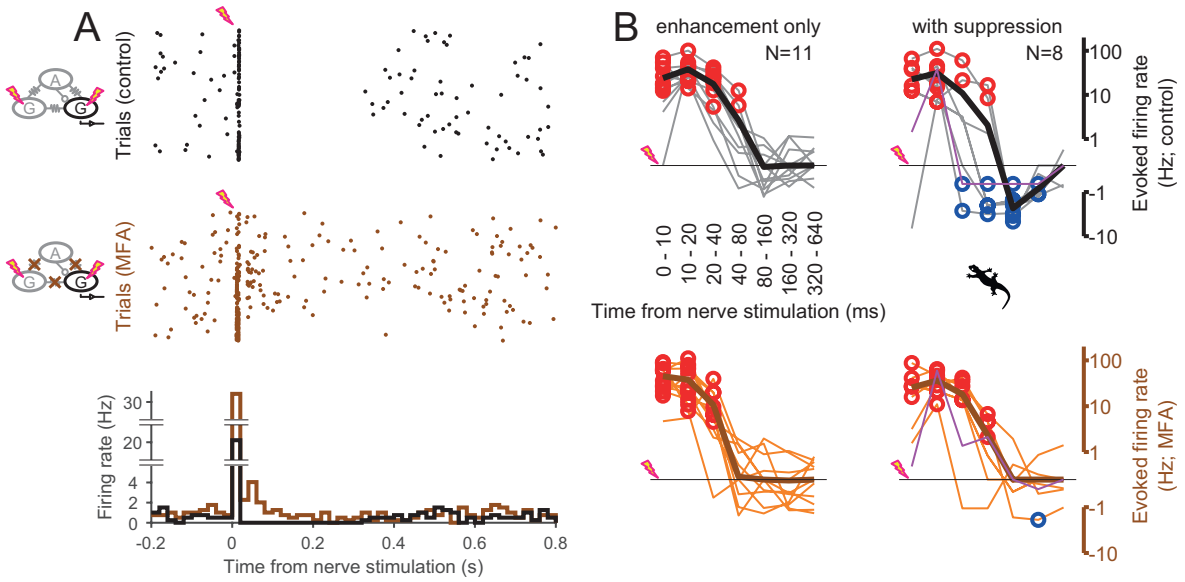
A
Trials (control)
Trials (MFA)
Firing rate (Hz)
30
20
4
2
0
-0.2
0
0.2
0.4
0.6
0.8
Time from nerve stimulation (s)
B
enhancement only
N=11
with suppression
N=8
0 - 10
10 - 20
20 - 40
40 - 80
80 - 160
160 - 320
320 - 640
Time from nerve stimulation (ms)
100
10
1
-1
-10
Evoked firing rate (Hz; control)
Evoked firing rate (Hz; MFA)

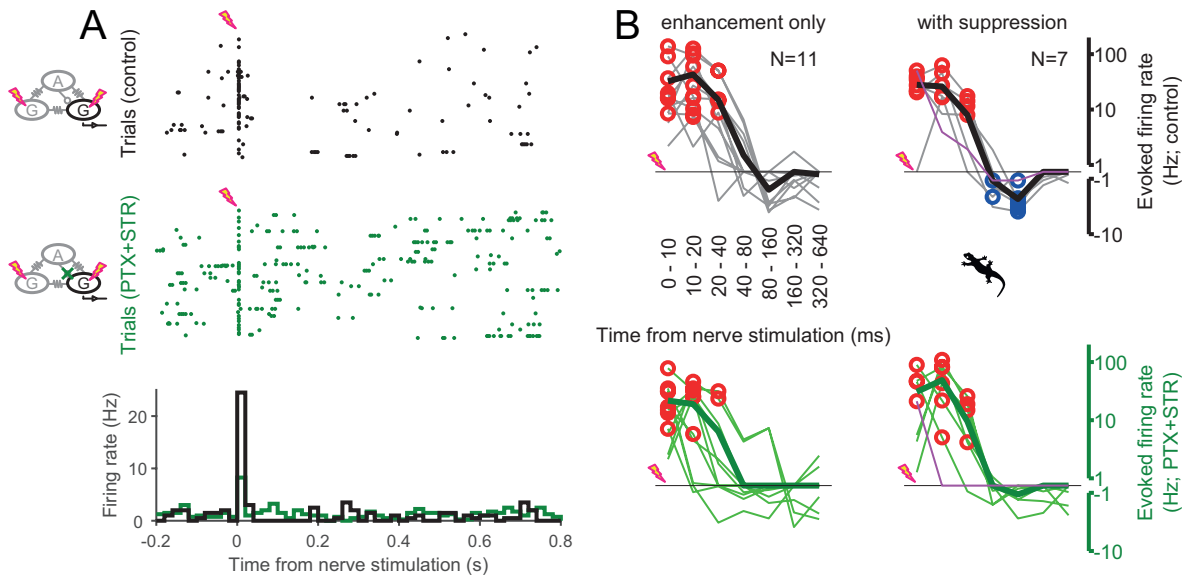
A
Trials (control)
Trials (PTX+STR)
Firing rate (Hz)
20
10
0
-0.2
0
0.2
0.4
0.6
0.8
Time from nerve stimulation (s)
B
enhancement only
N=11
with suppression
N=7
0 - 10
10 - 20
20 - 40
40 - 80
80 - 160
160 - 320
320 - 640
Time from nerve stimulation (ms)
100
10
1
-1
-10
Evoked firing rate (Hz; control)
Evoked firing rate (Hz; PTX+STR)

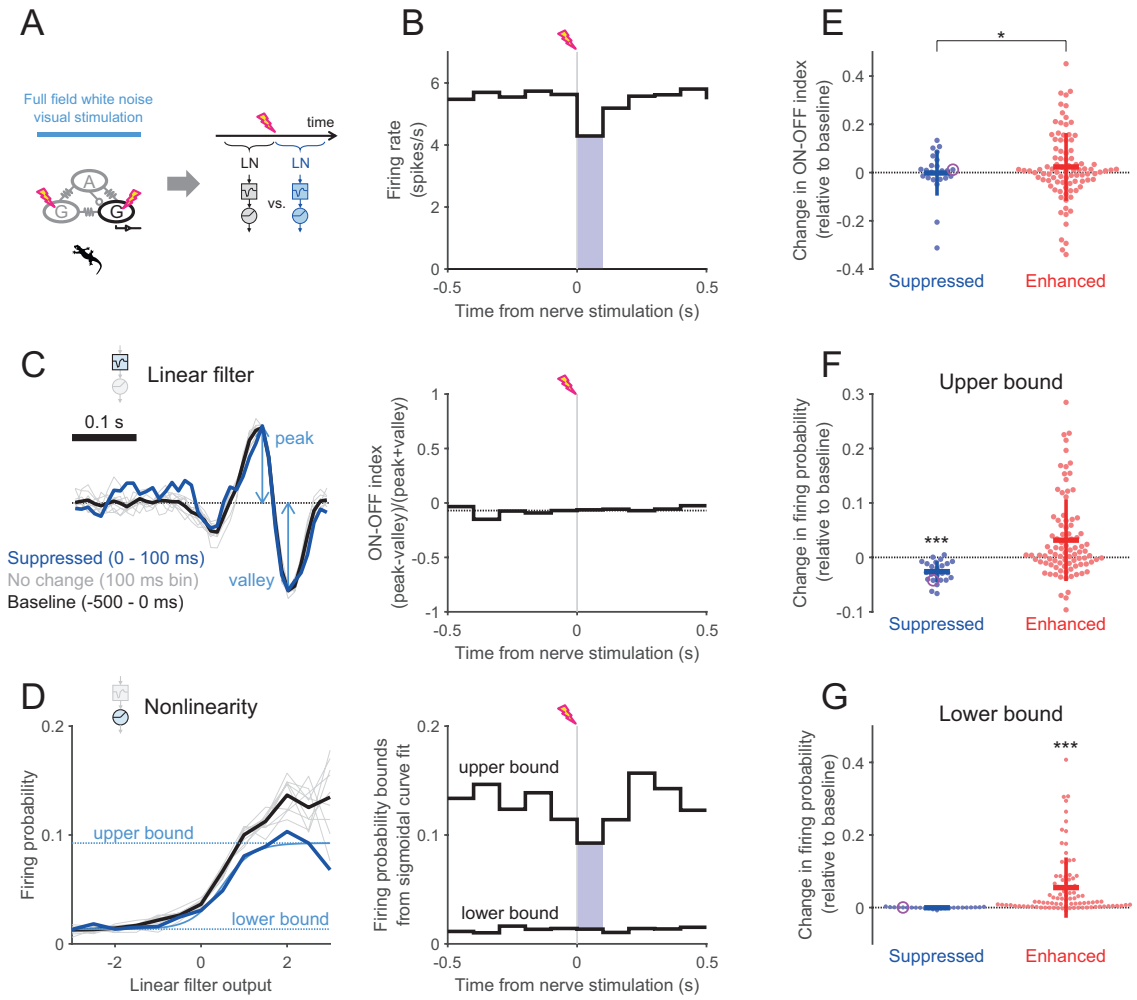
A
Full field white noise visual stimulation
A
G
G
time
LN
LN
vs.
B
Firing rate (spikes/s)
Time from nerve stimulation (s)
E
Change in ON-OFF index (relative to baseline)
Suppressed
Enhanced
C
Linear filter
0.1 s
peak
valley
Suppressed (0 - 100 ms)
No change (100 ms bin)
Baseline (-500 - 0 ms)
ON-OFF index (peak-valley)/(peak+valley)
Time from nerve stimulation (s)
F
Upper bound
Change in firing probability (relative to baseline)
Suppressed
Enhanced
D
Nonlinearity
Firing probability
upper bound
lower bound
Linear filter output
Firing probability bounds from sigmoidal curve fit
upper bound
lower bound
Time from nerve stimulation (s)
G
Lower bound
Change in firing probability (relative to baseline)
Suppressed
Enhanced

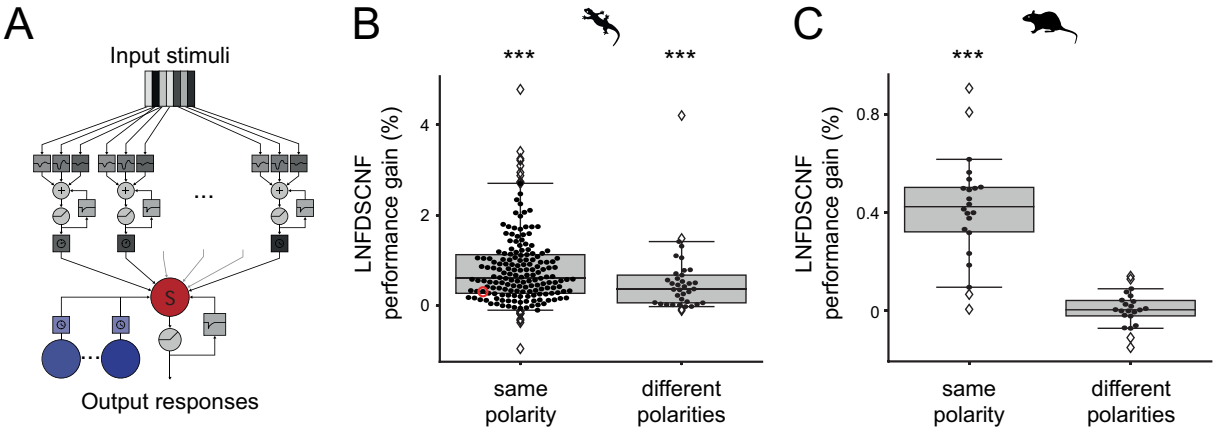
A
Input stimuli
S
Output responses
B
***
***
LNFDSCNF performance gain (%)
4
2
0
same polarity
different polarities
C
***
LNFDSCNF performance gain (%)
0.8
0.4
0
same polarity
different polarities

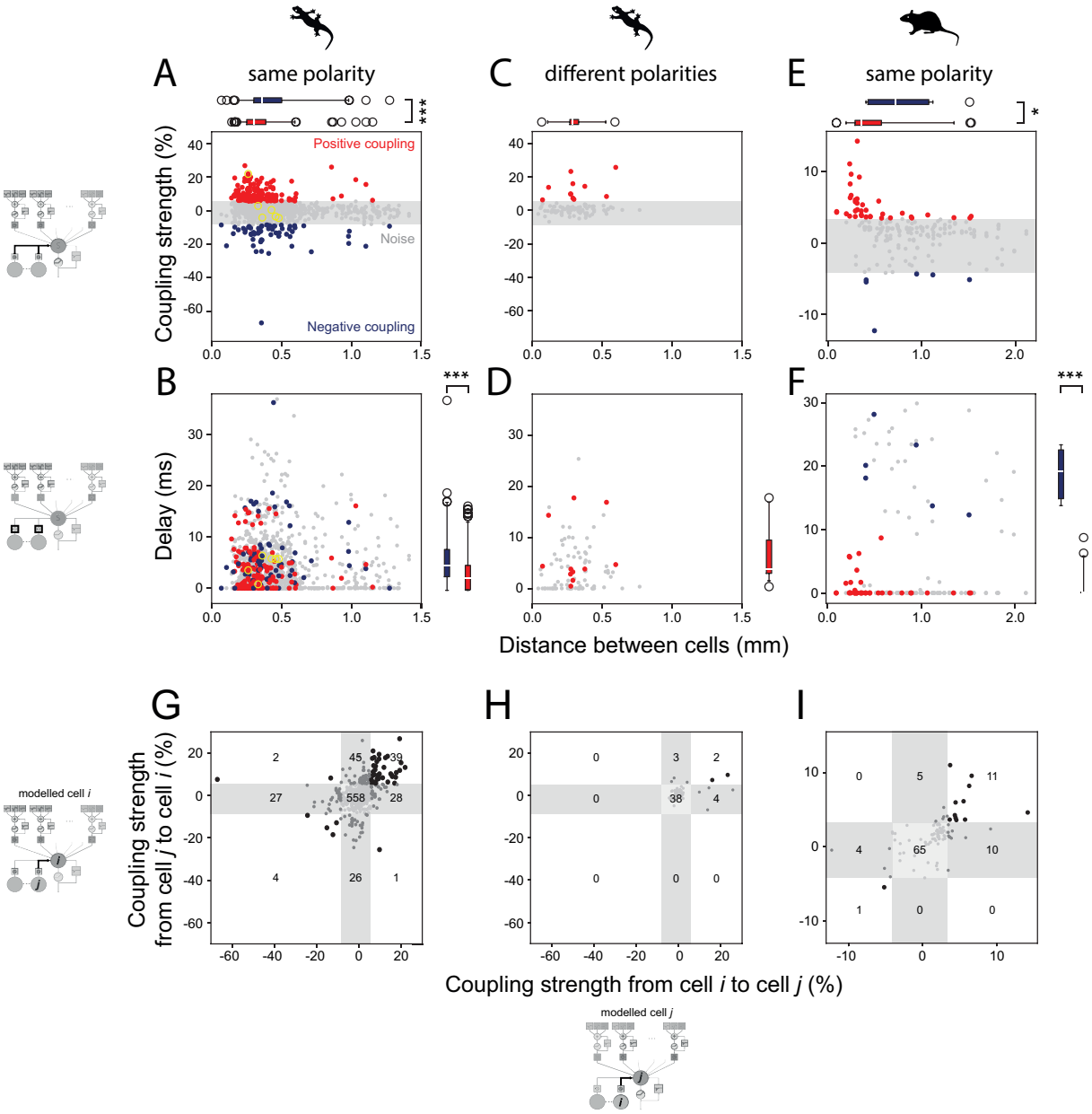
A
same polarity
C
different polarities
E
same polarity
Positive coupling
Noise
Negative coupling
Coupling strength (%)
B
D
F
Delay (ms)
Distance between cells (mm)
G
H
I
modelled cell i
Coupling strength from cell j to cell i (%)
Coupling strength from cell i to cell j (%)
modelled cell j

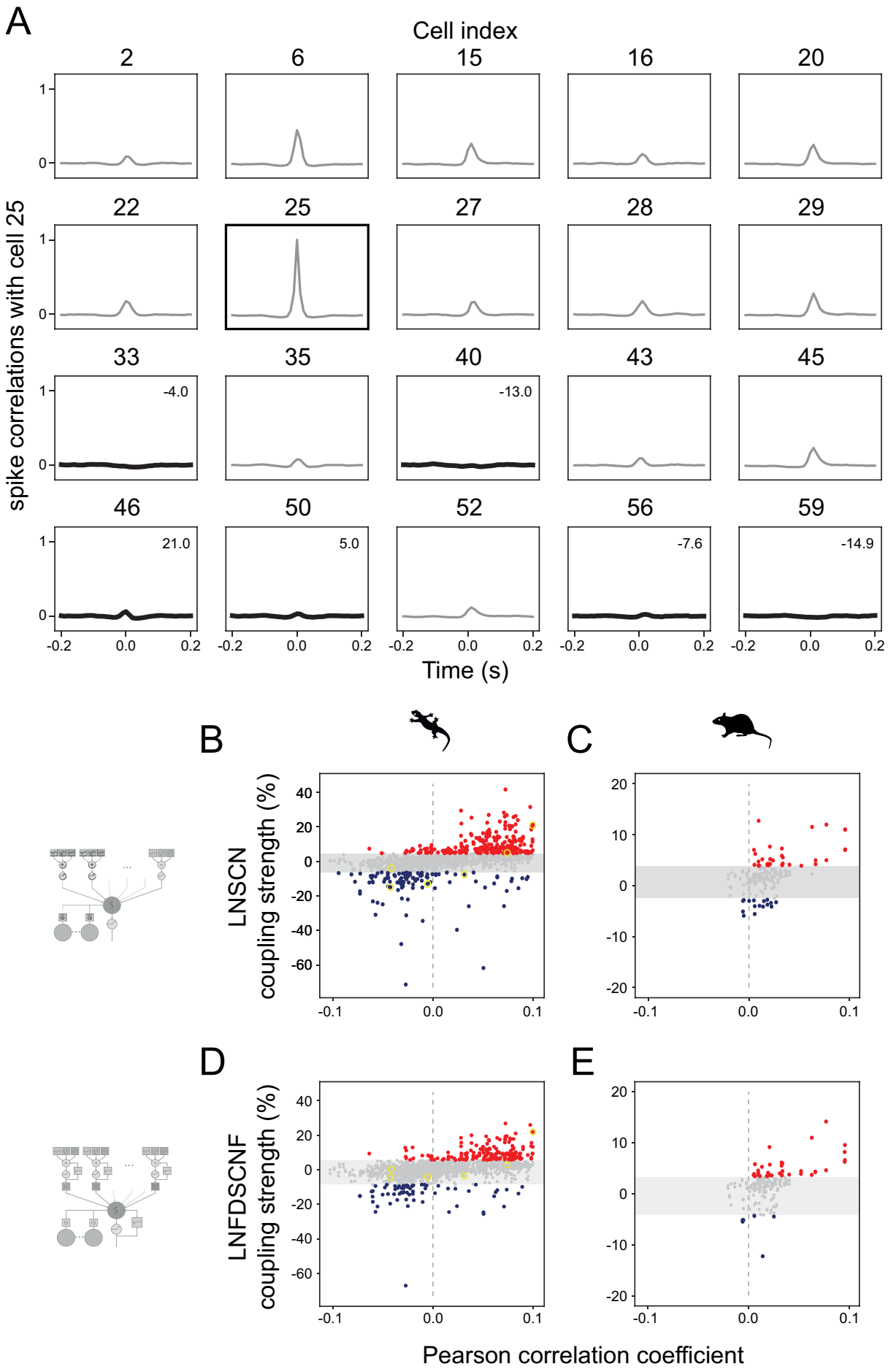
A
Cell index
2
6
15
16
20
22
25
27
28
29
33
35
40
43
45
46
50
52
56
59
-4.0
-13.0
21.0
5.0
-7.6
-14.9
spike correlations with cell 25
Time (s)
B
C
D
E
LNSCN coupling strength (%)
LNFDSCNF coupling strength (%)
Pearson correlation coefficient

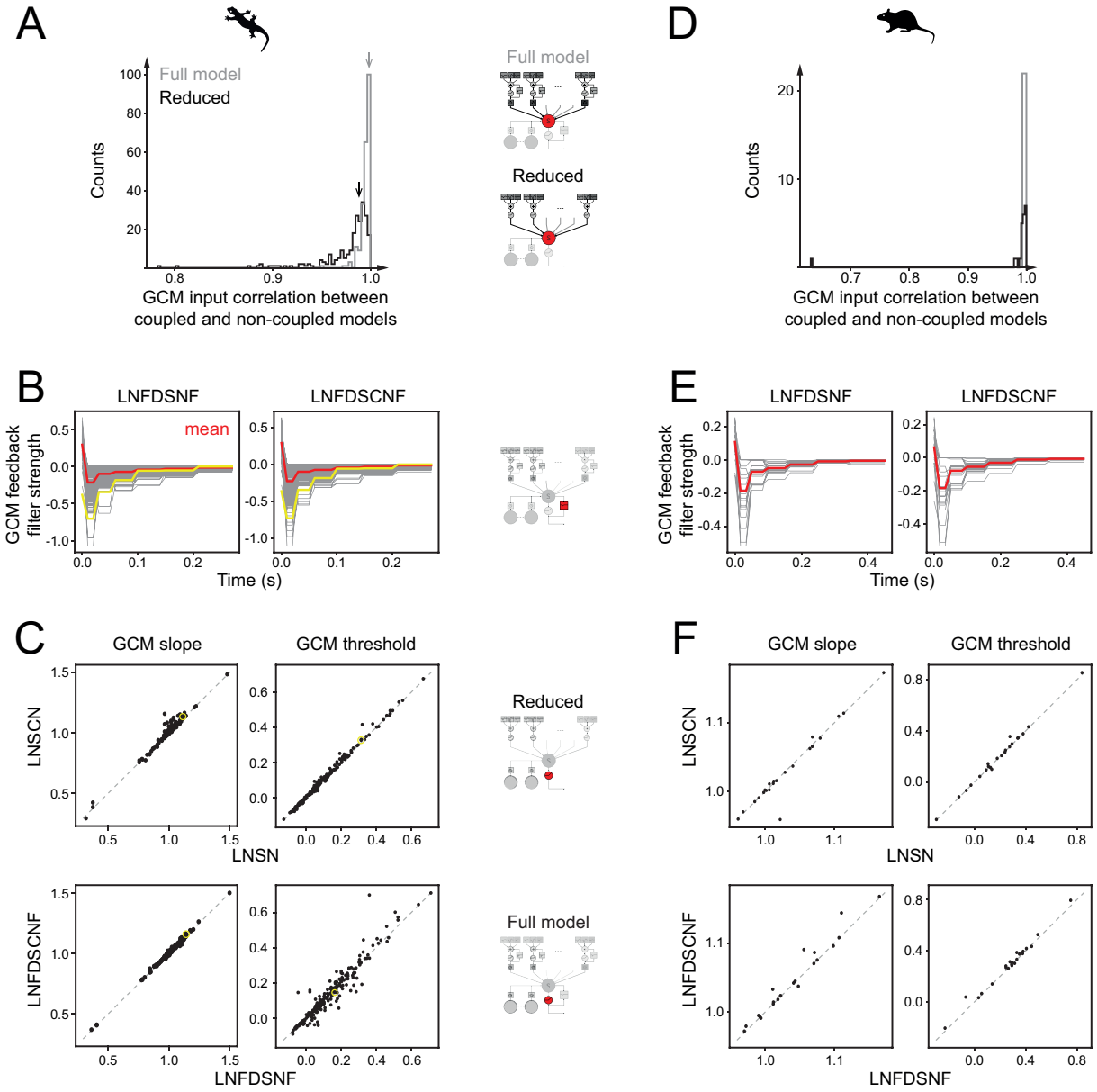
A
Full model
Reduced
Counts
GCM input correlation between coupled and non-coupled models
Full model
Reduced
D
Counts
GCM input correlation between coupled and non-coupled models
B
LNFDSNF
LNFDSCNF
mean
GCM feedback filter strength
Time (s)
E
LNFDSNF
LNFDSCNF
GCM feedback filter strength
Time (s)
C
GCM slope
GCM threshold
LNSCN
LNSN
Reduced
LNFDSCNF
LNFDSNF
Full model
F
GCM slope
GCM threshold
LNSCN
LNSN
LNFDSCNF
LNFDSNF

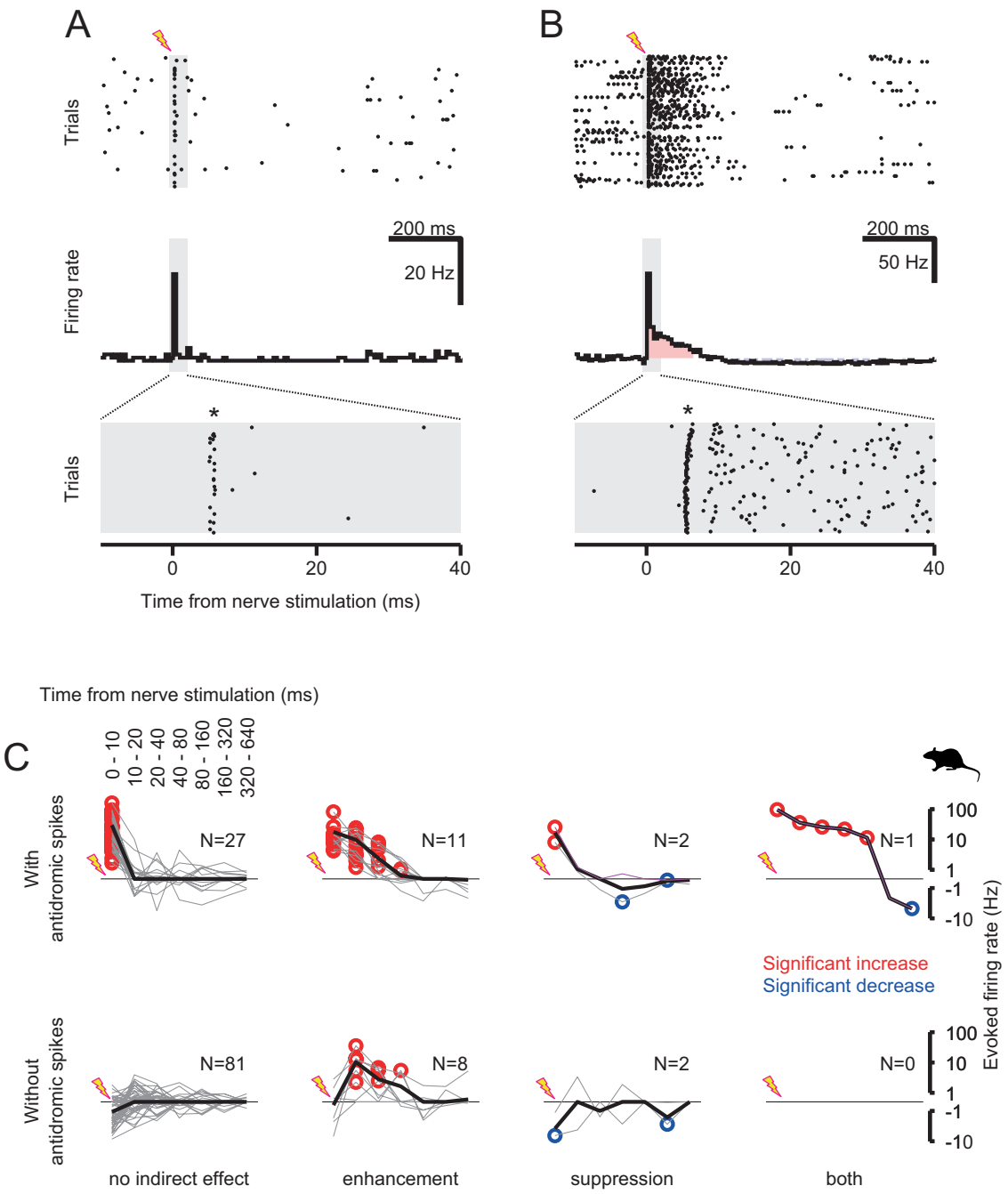
A
B
Trials
Firing rate
200 ms
20 Hz
50 Hz
Trials
0
20
40
Time from nerve stimulation (ms)
Time from nerve stimulation (ms)
C
0 - 10
10 - 20
20 - 40
40 - 80
80 - 160
160 - 320
320 - 640
With antidromic spikes
Without antidromic spikes
N=27
N=11
N=2
N=1
N=81
N=8
N=2
N=0
100
10
1
-1
-10
Evoked firing rate (Hz)
Significant increase
Significant decrease
no indirect effect
enhancement
suppression
both

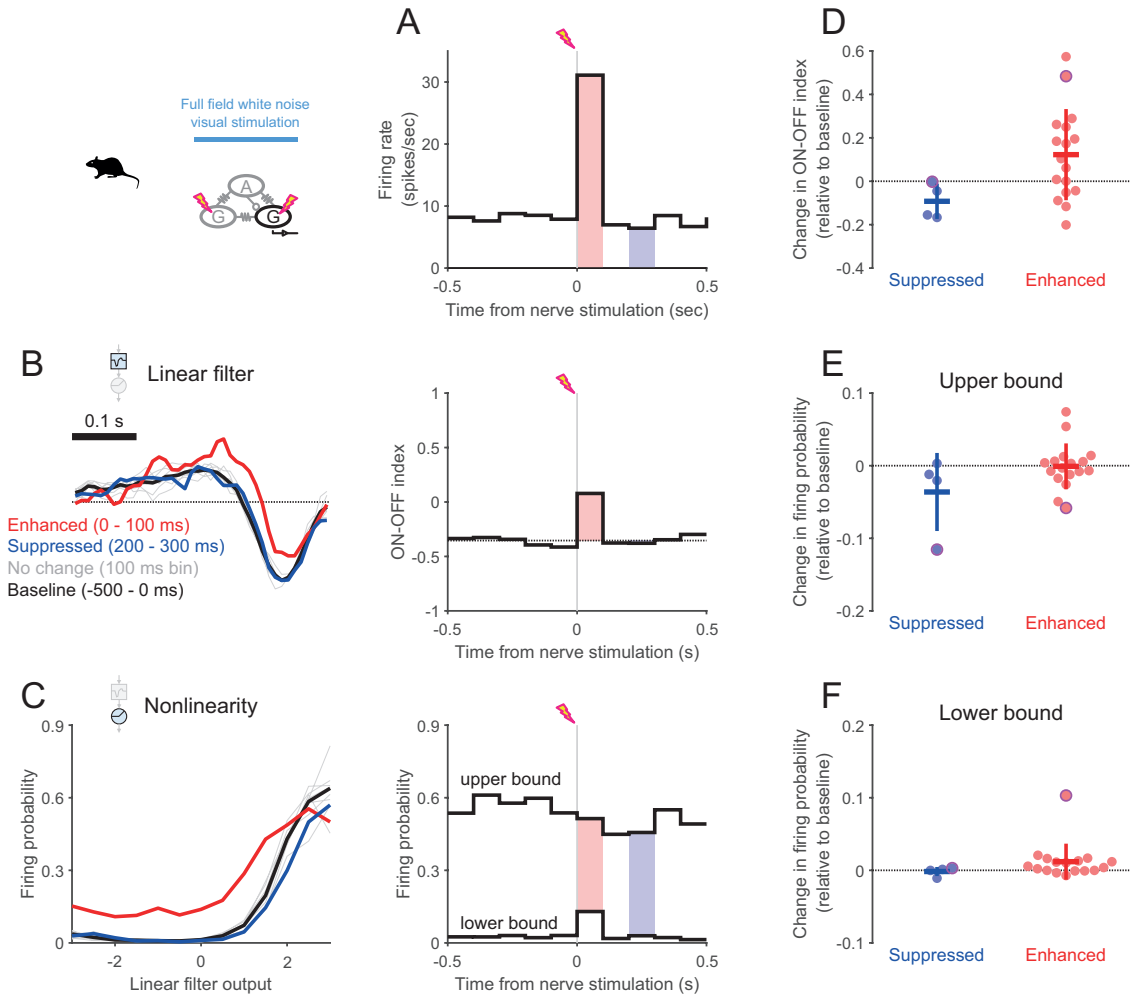
A
Full field white noise visual stimulation
A
G
G
Firing rate (spikes/sec)
Time from nerve stimulation (sec)
D
Change in ON-OFF index (relative to baseline)
Suppressed
Enhanced
B
Linear filter
0.1 s
Enhanced (0 - 100 ms)
Suppressed (200 - 300 ms)
No change (100 ms bin)
Baseline (-500 - 0 ms)
ON-OFF index
Time from nerve stimulation (s)
E
Upper bound
Change in firing probability (relative to baseline)
Suppressed
Enhanced
C
Nonlinearity
Firing probability
Linear filter output
upper bound
lower bound
Time from nerve stimulation (s)
F
Lower bound
Change in firing probability (relative to baseline)
Suppressed
Enhanced